ABSTRACT

KIM, JEE MYUNG. Characterization of Acoustic Wave Coupling between Cylindrical Waveguides for Sensing Applications (Under the direction of Dr. Kara Peters).

Fiber Bragg gratings (FBG) are often utilized as ultrasonic transducers for structural health monitoring (SHM) applications. Some of the greatest challenges in utilizing FBG sensors are that the system is hard to expand once installed because the sensor locations are fixed, and that it requires numerous sensors to cover large areas because ultrasonic waves attenuate over distance.

Recently, researchers have investigated collecting and propagating acoustic waves through optical fibers for SHM applications. There is the possibility to use these acoustic waves to expand the FBG sensor network by coupling multiple optical fibers together.

Fused optical couplers have been utilized to transfer acoustic waves from one optical fiber to another. However, they are complicated to fabricate and may not be suitable in field applications. In more recent studies, acoustic couplers using an adhesive bond to attach the surfaces of the two fibers were investigated. Using this simple adhesive acoustic coupler, a segment of sensing fiber can be coupled to an already installed sensing fiber to transfer the wave, thus easily extending the system to cover larger areas without having to introduce new channel of sensors.

In this dissertation, the behaviors of acoustic coupling via an adhesive coupler are experimentally investigated and an analytical model that best describes the behaviors is compared to the results. We experimentally demonstrate that the diameter ratio of input to output fiber for maximum energy transfer is not 1.0 as predicted in previous studies, and that the modulus mismatch between input and output waveguides decreases the energy transfer. Experimental results show that the energy transfer increases as the cross-sectional area of the input fiber increases, until the diameter mismatch between input and output fiber becomes significantly large

and then the energy transfer decreases. We also experimentally demonstrate that the acoustic wave coupling through the adhesive coupler is coherent. We then construct a finite element analysis (FEA) model, verified with the experimental results. This model is compared with an analytical model to investigate if the analytical model properly represents the actual acoustic coupling via the adhesive coupler. Lastly, we experimentally demonstrate extending a sensor system by attaching a segment of optical fiber to the environment and coupling it to the already installed sensor fiber using an adhesive coupler, enabling it to detect damages that were otherwise undetectable. The results of this research demonstrate that the optical fiber sensing system can be effectively extended to cover larger areas using adhesive acoustic couplers.

Characterization of Acoustic Wave Coupling between Cylindrical Waveguides for Sensing Applications

by
Jee Myung Kim

A dissertation submitted to the Graduate Faculty of
North Carolina State University
in partial fulfillment of the
requirements for the degree of
Doctor of Philosophy

Mechanical Engineering

Raleigh, North Carolina
2022

APPROVED BY:

_____	_____
Kara Peters Committee Chair	Landon Grace
_____	_____
Cheryl Xu	Michael Kudenov

DEDICATION

This research work is dedicated to my parents, Byung Hyun Kim and Jin Sook Ahn, who have always been there by my side and supported me during the good and bad times. They were always the perfect examples to follow, and without their sacrifice and guidance I would not be the person I am today.

BIOGRAPHY

Jee Myung Kim received the Bachelor of Science degree in Mechanical Engineering from Calvin University in 2015. After 3 years of work experience in the automotive industry as an engineer, he joined the combined M.S/Ph.D. program in Mechanical and Aerospace Engineering at North Carolina State University (NCSU) in year 2018. At NCSU he studied and worked as a graduate student in Smart Composite Laboratory under the guidance of Dr. Kara Peters.

ACKNOWLEDGMENTS

I would like to express my sincerest appreciation to Dr. Kara Peters for her passionate and insightful guidance throughout my graduate years. Without her I would not have been able to come this far. I am very fortunate to have her as my advisor because the past years as a graduate student under her guidance truly shaped the person that I am today.

I greatly appreciate my committee members, Dr. Landon Grace, Dr. Cheryl Xu, and Dr. Michael Kudenov, for their encouragement and advice during my graduate study.

I would like to extend my appreciation to the members of the Smart Composites Laboratory; Dr. Junghun Wee, Dr. Chia-Fu Wang, Cameron Marashi, Anastasia Timofeeva, Sherif Hassan Aboubakr, Sean Aiton, Alex Boyer, and Evan Youngberg. I am truly grateful that we could spend time together and share great ideas in this laboratory. I especially would like to thank Dr. Junghyun Wee for his advice and feedbacks during his time here as a postdoctoral research scholar, and those feedbacks truly helped me to succeed in my research.

Finally, I would like to appreciate the Office of Naval Research (ONR) for the financial support of this research.

TABLE OF CONTENTS

LIST OF TABLES

LIST OF FIGURES

CHAPTER 1

Introduction

1.1 Background

Structural health monitoring (SHM) is the general term for observation and analysis of a system using periodically sampled response measurements to monitor defects and predict the residual life of the structure. One of the methods used in SHM is the ultrasonic pitch-catch method. In this method, an actuator excites guided waves in the structure and a detector at a distance away detects the wave. When damage occurs between the actuator and the detector, the guided wave becomes distorted, and by comparing it to the undistorted wave, the information about the damage can be found such as location and the severity of the damage [1, 2].

In case of a thin-walled structure, ultrasonic waves travel through the structure as guided Lamb waves [3]. Lamb waves are elastic and can travel over large area with little energy loss, which is ideal for SHM applications. There are two types of Lamb wave modes: symmetric (S) and antisymmetric (A) modes, which are characterized by their waveforms. Specifically, the displacement of S mode is symmetric about the neutral axis of the medium and that of A mode is antisymmetric about the neutral axis. The wave speed of the Lamb waves can be found using the wave frequency and the thickness of the structure. Figure 1.1. shows the dispersion curves of aluminum plate for Lamb waves. Higher order modes of Lamb waves can simultaneously exist for higher product of wave frequency and structure thickness. However, this dissertation only focuses on the fundamental symmetric (S_0) and antisymmetric (A_0) modes due to the complexity of demodulating different modes.

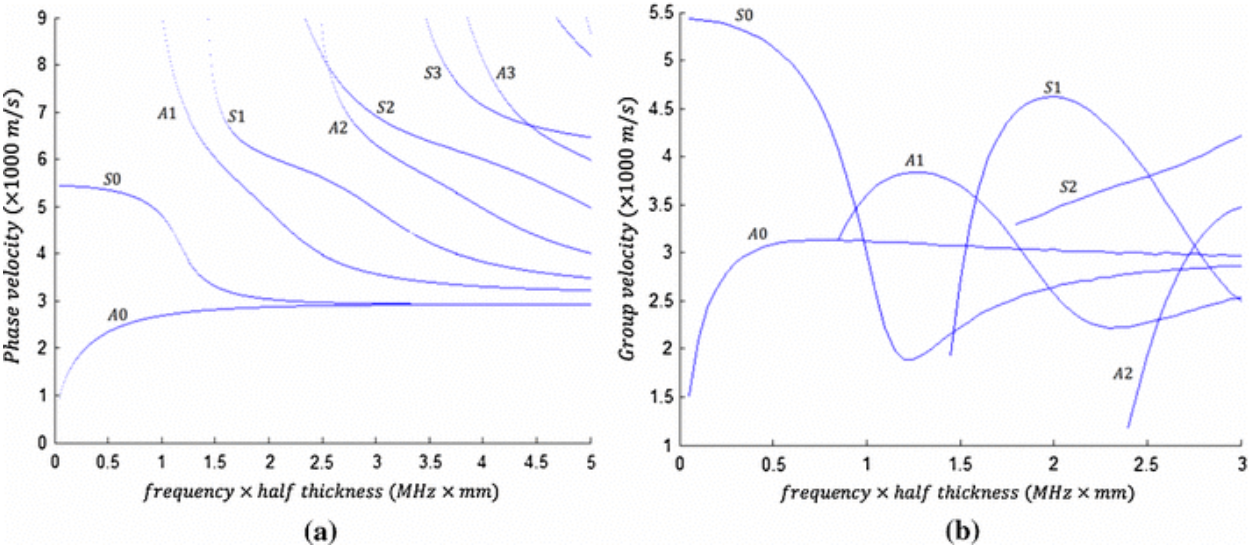

Figure 1.1 (a) Calculated phase velocity and (b) group velocity dispersion curves of aluminum plate [4].

Fiber Bragg grating (FBG) sensors are one of the most widely used ultrasonic transducers for the measurement of Lamb wave signals in SHM applications. Perez et al. [5] and Betz et al. [1] demonstrated the detection of Lamb waves in thin structures using FBG sensors. They were some of the first researchers that demonstrated the potential to utilize FBG sensors for damage monitoring. Tsuda [6] utilized FBG sensors on impact-damaged carbon fiber reinforced plate (CFRP) to detect Lamb waves and inspect the damage. The piezo-electric transducer (PZT), damage location, and FBG sensor were aligned. The FBG was used to detect the Lamb waves excited from the PZT with and without the presence of the damage to analyze the change in the FBG response. More recently, Frieden et al. used multiple surface bonded FBG sensors to perform damage localization [7].

1.2 Fiber Bragg Grating Sensors

The FBG is a narrow band wavelength filter embedded in an optical fiber. When broadband light encounters the FBG, certain narrow bandwidth of light is reflected, and the rest of the wavelengths are transmitted as shown in Figure 1.2. The FBG is structured such that the refractive index of the core of the optical fiber is periodically perturbed along the grating length, which allows such reflection. The reflection is a spectrum of wavelength centered at a characteristic wavelength called Bragg wavelength (λ_B), and is defined by:

$$\lambda_B = 2n_{eff}\Lambda \tag{1.1}$$

where n_{eff} is the effective refractive index of the fundamental mode and Λ is the grating period [9]. When axial strain is applied to the FBG, the periodic modulation of the grating changes and as a result the Bragg wavelength changes. Under compressive strains the Bragg wavelength shifts to lower wavelength, and under tensile strain the wavelength shifts to a higher wavelength. The shift in Bragg wavelength is linearly related to the applied axial strain by:

$$\frac{\Delta\lambda_B}{\lambda_B} = (1 - p_e)\varepsilon \tag{1.2}$$

where p_e is the photo-elastic constant for a fused silica optical fiber, and ε is the applied axial strain. This allows the FBG to couple ultrasonic wave signals to optical signals.

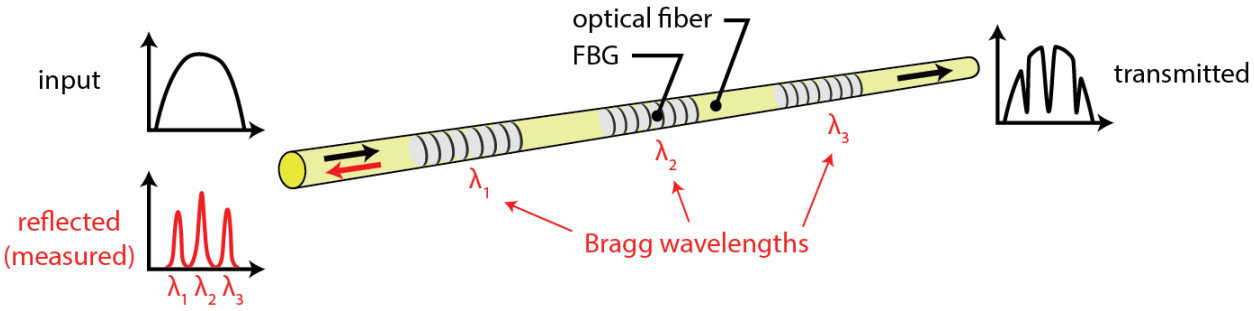

Figure 1.2 Operation principle of FBG [8].

To efficiently detect Lamb waves the FBG must be able to measure high frequency and small amplitude strains. The most commonly used FBG demodulation technique for this application is called edge filtering, which is shown in Figure 1.3. Figure 1.3(a) shows the principle of edge filtering technique and Figure 1.3(b) shows the edge filtering setup. The output wavelength of the narrowband tunable laser is initially set to the mid-point of the FBG ascending edge of the reflected spectrum. When strain is applied to the optical fiber, the Bragg wavelength increases or decreases. This changes the reflected optical power from the FBG, which is measured using the photodetector. By using the voltage output measured by the oscilloscope, the reflected spectrum of FBG, and the spectral edge slope, the strain amplitude on the FBG can be calculated.

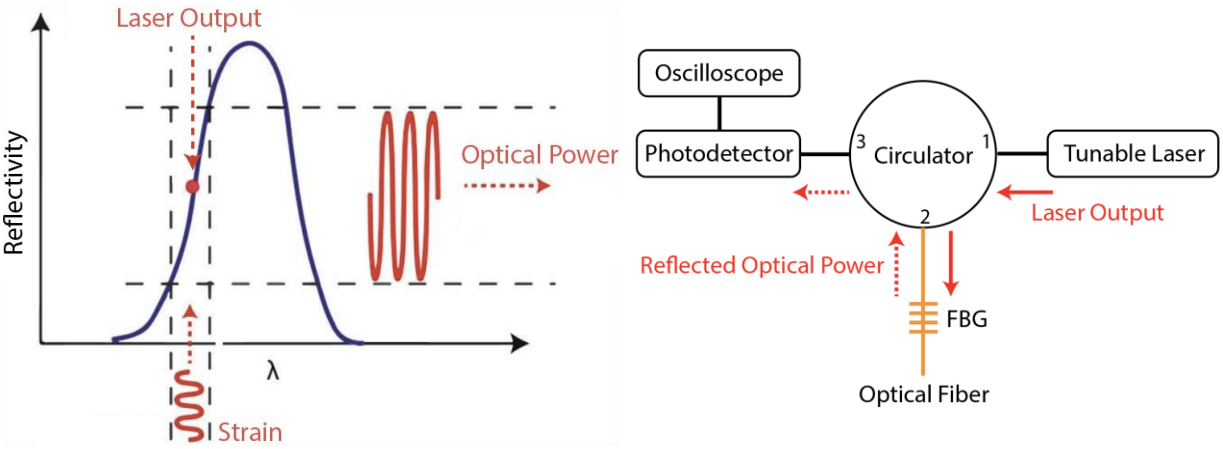

(a) (b)

Figure 1.3 (a) Principle of edge filtering technique and (b) edge filtering setup.

One of the greatest advantages of utilizing FBG sensors in SHM applications is its ability to multiplex multiple FBG sensors in a single optical fiber. This means that multiple sensing locations can be covered with only a single lead-in lead-out connection. Also, FBG sensors are resistant to corrosion and magnetic interferences, which means it can be applied in harsh environments.

One of the greatest challenges in utilizing FBG sensors in SHM of large structures is that the sensor locations are fixed once the optical fiber is installed to the structure. Therefore, a large number of FBG sensors are needed to cover large area, including potential regions where "hot spots" could occur in the structure. If such "hot spots" occur in unexpected locations where sensors are not installed, the installed network cannot be reconfigured to measure emissions or signals in the new region. If new sensors are to be installed, then a new sensor channel must be introduced to the network by cleaving and splicing optical fibers to the installed network, which is not practical in most field applications, as the fiber is typically bonded to the structure. This is also the challenge addressed in this dissertation.

1.3 Expanding the System by Multiplexing using Acoustic Couplers

1.3.1 Remote Bonding of FBG Sensors

FBG sensors are typically exposed directly to ultrasonic waves, which induce axial strain in the FBG and cause a perturbation to the reflected spectrum. However, researchers have recently demonstrated that ultrasonic waves in a structure can also be coupled into an optical fiber, converted into propagating longitudinal waves, and measured with an FBG at a remote location further along the optical fiber [10,11]. Using this remote bonding configuration, the signal amplitude detected by the FBG can be significantly increased [10]. In this configuration, the fundamental symmetric (S_0) and antisymmetric (A_0) Lamb waves in a structure have been shown to be converted to fundamental longitudinal (L_{01}) traveling waves in the optical fiber through an adhesive bond. Furthermore, these traveling waves can be transferred from one optical fiber to another by joining them along a short segment, called couplers [12]. Therefore, multiple optical fibers could potentially be used as ultrasound detectors at different locations and joined together through an acoustic coupler to merge the extracted signals and measure them with a single FBG sensor. In other words, remotely bonded FBG sensors could be multiplexed to a single interrogator.

1.3.2 Previous Works on Optical Fiber Acoustic Couplers

Since the longitudinal mode has a similar form to the fundamental optical mode, standard fused optical couplers have been investigated as acoustic couplers for sensing applications. Most commonly, the coupler is exposed directly to the ultrasonic signal, and the acoustic wave perturbs the coupling ratio of the optical coupler, which is detected by measuring the power at the different coupler outputs [13–16]. Chang et al. [13,14], Chen et al. [15], and Li et al. [16] produced an optical coupler by stretching two single-mode optical fibers under a heat source and fusing them. Similarly, Wang et al. [17] manufactured a coupler-based sensor by heating two fibers without

stretching them. In these configurations, the optical coupling is well represented by coupled-mode theory [18], but acoustic coupling from one optical fiber to another is not present.

Fewer studies have investigated the use of a coupler to transfer acoustic waves from one optical fiber to another. Matthews et al. [12] evaluated an acoustic fiber waveguide coupler fabricated by twisting and heating two identical fibers. They observed that the splitting efficiency and excess loss parameters of the coupler improved when the fused region of fibers is long and gradual. Matthews et al. [12] also successfully demonstrated an acoustic fiber waveguide coupler, but noted the high insertion loss, high excess losses, and asymmetrical power splitting.

The optical modes are confined near the core of the fiber, therefore when creating an optical coupler it is necessary to fuse the two fibers so their cores are in close contact. However acoustic modes are spread out across the fiber cross-section, so fusing the fibers to the core level is not necessary. Instead, the two fiber surfaces could be simply bonded together using adhesives to couple acoustic waves. Since this does not require a fusing process, fibers of different sizes and kinds can be coupled together, meaning the sensing fiber exposed to the environment does not have to be a standard single-mode fiber.

Leal et al. [19] experimentally demonstrated a fiber-optic ultrasonic splitter using adhesive bonds to couple acoustic waves from one fiber to another. The sequence of experimental setup and averaged result are shown in Figure 1.4. Figure 1.4(a) shows a segment of single-mode fiber glued to the main single-mode fiber at two locations using cyanoacrylate (CA) adhesive. An ultrasound wave is excited on the main fiber, and 7.6 mV_{pp} was measured on the opposite end of the main fiber. In Figure 1.4(b), a load was applied on the main fiber before the splitter, and the measured voltage dropped to 0.6 mV_{pp}. Then in Figure 1.4(c), the load was moved to the main fiber between the splitter, and the measured voltage increased to 3.2 mV_{pp}, indicating that a fraction of the

ultrasound energy rerouted through the glued fiber and recoupled to the main fiber. Lastly Figure 1.4(c) shows that when the load was applied over the main fiber and the splitter, the measured voltage dropped back down to less than 1 mV_{pp}.

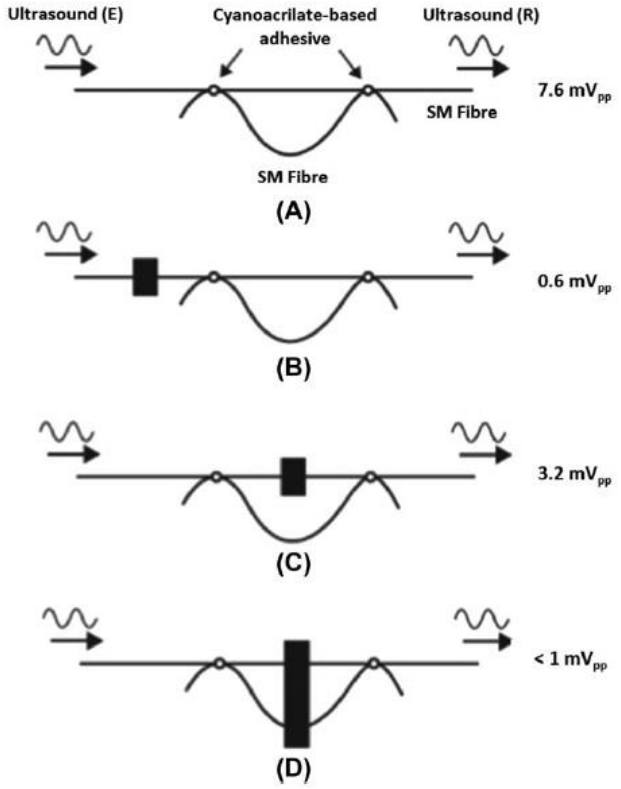

Figure 1.4 Series of experimental setups and averaged results for fiber-optic ultrasonic splitter [19].

In addition to fabricating the acoustic coupler and measuring its behavior, it is also important to be able to predict the performance of the acoustic coupler. Safaai-Jazi [20] theoretically studied the exchange of acoustic power between two dissimilar parallel cylindrical acoustic waveguides with a common cladding, following the coupled-mode theory used for lightwave coupling in fused couplers. He predicted that when the two fibers are identical, complete

transfer of power from one fiber to another is possible. He also predicted that when the fiber diameters are different, a fraction of the total power oscillates between the fibers [20]. However, the accuracy of the coupled-mode theory for the acoustic coupling was not experimentally verified.

1.4 Scope of Research

The goal of this work is to investigate acoustic coupling of ultrasonic waves from one waveguide to another using a simple adhesive bond, to theoretically analyze the key coupling parameters, to demonstrate multiplexing of FBG sensors using acoustic couplers in field-application-like scenarios, and to develop numerical and finite element models to compare with theoretical model. The specific research objectives are:

1. Develop an experimental method to measure the acoustic coupling efficiency between two fiber waveguides.
2. Generate experimental data sets on coupling energy efficiency for a wide range of fiber waveguide combinations.
3. Experimentally investigate the coherence of acoustic wave coupling through the adhesive bond.
4. Demonstrate the use of acoustic coupling for multiplexing remotely bonded sensors for SHM applications.
5. Develop a numerical and finite element model of the coupling process for comparison with the theoretical model.

Chapter 2 presents the modeling of the acoustic coupler using an adhesive bond, and experimentally demonstrates acoustic coupling from one waveguide to another. A metal mold is designed and manufactured to ensure consistency in fabrication of the adhesive bond. Acoustic waves are excited on a standard input fiber and coupled to an output waveguide with varying

diameters, geometries, and materials. The results demonstrate that coupling two waveguides through an adhesive bond allows the coupling of acoustic waves between them, which allows rapid connection of fibers to optical fibers containing sensors in field applications. It also demonstrates that waveguides of different diameters, geometries, and materials can be coupled to a standard polyimide coated silica optical fiber, meaning the fiber used to collect the acoustic wave does not have to be an optical fiber.

Chapter 3 investigates the coherent interference between acoustic waves using a fiber ring resonator made from adhesive acoustic coupler. A segment of optical fiber is cleaved and spliced to fabricate a ring, and coupled to the main fiber using an adhesive bond. The optical fiber is varied in sizes and geometries. The results demonstrate that the acoustic waves transferring through an adhesive coupler interfere coherently, and that the interference pattern follows the theoretical model of optical ring resonator.

Chapter 4 experimentally demonstrates an easy method to extend an already installed sensing network by attaching optical fibers to the structure using adhesive and coupling it to the fiber with sensor using adhesive coupler. The results show that the sensor is able to detect the damage occurring in locations that are otherwise unable to detect.

Chapter 5 develops a numerical and finite element model of acoustic coupler using COMSOL Multiphysics software and compares the results with the theoretical model of acoustic coupling. The results show that the Spring Model which produces similar results as the Coupled Mode Theory works well in properly modeling the acoustic coupling.

Lastly, Chapter 6 summarizes the results drawn from this research and addresses recommendations for future work.

CHAPTER 2

Acoustic Wave Coupling Between Optical Fibers of Different Geometries

In this study, we investigate coupling of acoustic guided waves from different types of input fibers, through a bonded coupler, to an optical fiber. These acoustic waves can then be detected with conventional fiber Bragg gratings (FBGs). The input waves are measured using a high-resolution 3D laser Doppler vibrometer, and the output waves in the optical fiber are measured using an FBG. We demonstrate that the wave coupling between two waveguides varies with the cross-sectional area and the modulus of elasticity of the fibers

2.1 Introduction

Fiber Bragg gratings (FBGs) are often utilized to detect ultrasonic waves for structural health monitoring (SHM) applications. They are immune to electromagnetic interference, which for some applications can overwhelm signals collected by piezo-electric (PZT) material detectors [8,21]. In addition, large numbers of sensors can be multiplexed in a single fiber, which means that they can be embedded in material systems with minimal loss of structural integrity.

This paper experimentally investigates the acoustic wave transfer between two optical fibers with different cross-section geometries or different material properties. Transferring the acoustic waves between multiple fiber types means that the fiber exposed to the measurement environment does not have to be a standard single-mode optical fiber in order to support a FBG. Fusing of the silica optical fibers is necessary when the coupler is required to transfer lightwaves between the two fibers. However, if only acoustic coupling between the two fibers is required, simpler fabrication techniques can be used with similar results, such as adhesive bonding of the optical fibers [19]. We therefore fabricate the acoustic coupler based on bonding the two fibers using a custom-made mold. Using an adhesive bond permits coupling of different fiber types,

beyond silica optical fibers. We experimentally investigate the wave transfer through the acoustic coupler, demonstrating that the wave transfer varies as a function of the cross-sectional area and the modulus of elasticity of the input fiber.

2.2 Experimental Setup

The goal of the experiments in this paper is to measure the coupling efficiency of acoustic waves from one fiber waveguide to an optical fiber (we label these the input fiber and output fiber) through a coupler. Specifically, we launch input ultrasonic L01 waves into the input fiber, which are then coupled into the output fiber through the acoustic coupler. The output fiber is a standard 125 μm single-mode polyimide coated silica optical fiber for all experiments. Three different kinds of input fibers were used in the experiment: solid silica fibers, hollow silica fibers, and solid metallic fibers. An overview of the setup to measure the coupling efficiency is shown in Figure 2.1.

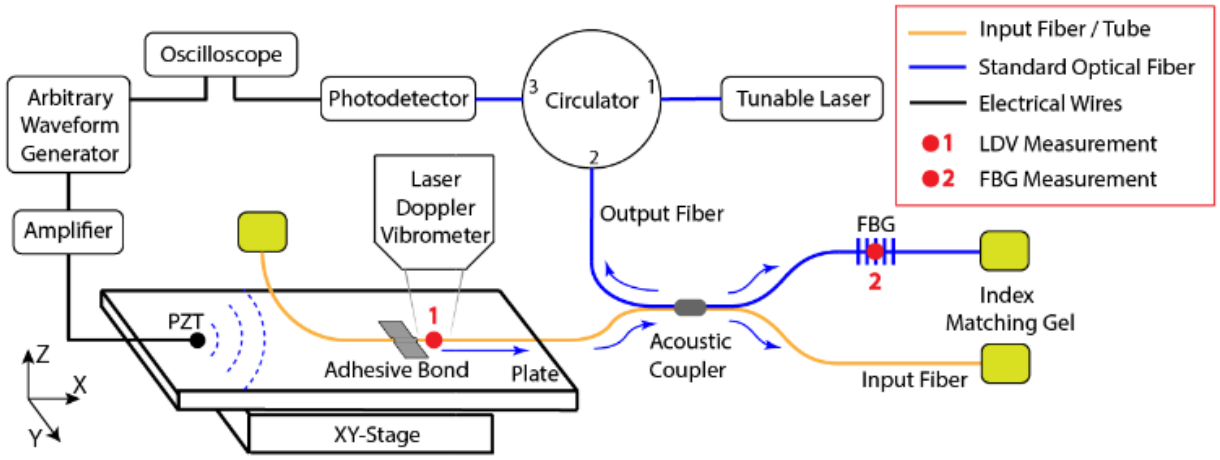

Figure 2.1 Setup of the acoustic coupler experiment, with acoustic wave paths shown as blue arrows and measurement locations shown as red dots.

Input L01 ultrasonic waves were launched in the input fiber by bonding it to an aluminum plate and generating Lamb waves in the plate, which are converted to L01 waves at the bond [22].

As the amplitude of the L01 wave coupled into the input fiber depends on the fiber geometry, we measure the input waves launched in the input fiber using 3D laser Doppler vibrometry (LDV). The use of LDV to accurately measure the amplitude of guided traveling waves in optical fibers was previously demonstrated in [22]. While this launching method was not optimized for maximizing wave coupling into the input fiber, it produced sufficient input wave amplitude and was compatible with measuring the input waves using the LDV. The amplitude of the output L01 waves in the output fiber are measured using an FBG, an easier detection method. FBG sensors are only available in the standard single-mode optical fibers; therefore, we cannot use this detection method to measure the input wave amplitude in the input fibers. The input-to-output wave amplitude ratio for the acoustic coupler is calculated from these measurements.

A 300 kHz PZT actuator was glued onto the 6061 aluminum plate with the dimensions of 609.6 mm × 609.6 mm and 0.8 mm thickness using cyanoacrylate (CA) adhesive. It was previously demonstrated that CA adhesive well transfers Lamb waves in the structure to traveling waves in the optical fiber through the adhesive bond [10,11,22]. The plate boundaries were covered with an elastomeric damping material (Dynamat) to reduce boundary reflections. The input fiber was attached to the plate by a thin layer of 2 cm width by 1 cm length CA adhesive bond. The adhesive bond is located 15 cm away from the PZT. To ensure consistency and repeatability of the adhesive bonds, a rectangular area of 2 cm width by 1 cm length was marked with Kapton tape over the fiber on the plate, and CA adhesive was spread over the area using a scraper. The Kapton tape was removed after curing the adhesive for 24 hours. The acoustic coupler is located 15 cm away from the plate adhesive bond location, where the input and output fibers are coupled. On the output fiber, an FBG sensor with 1588 nm Bragg wavelength and 10 mm length is located 15 cm away from the acoustic coupler. During the experiment, all loose ends of the fibers were submerged in

index matching gel to minimize optical reflections. In addition, the gel diffused the acoustic waves, preventing reflections back into the optical fiber.

The S_0 Lamb waves were generated in the plate by sending a 300 kHz, Hanning windowed function of 5.5 cycles to the PZT from an arbitrary waveform generator (AWG) through an amplifier. The input excitation signals from the AWG were time synchronized with the measurement acquisition by a transistor– transistor logic (TTL) trigger signal. The S_0 mode waves are coupled to the L_{01} waves in the input fiber through the adhesive bond. F_{11} modes in the optical fiber are also generated at the adhesive bond on the plate and the adhesive coupler, however, these decay rapidly along the optical fiber. The FBG on the output fiber also can only detect L01 modes.

The input L_{01} modes were measured at location 1, as indicated in Figure 2.1 with a red dot. While LDV can provide accurate measurements of L_{01} wave amplitudes in optical fibers, its implementation is more complex, and the measurements have more noise than those of the FBG sensor [22]. However, the input fiber varied in size and type and was not necessarily compatible with FBG sensor fabrication. The LDV setup is shown in Figure 2.2(a). The LDV sensor head was stationary, and the aluminum plate was placed on the XY stage that moves in the XY plane following the XYZ coordinate system specified in Figure 2.2(b). The XY stage positioned the aluminum plate such that the laser emitted from the LDV sensor head could be directed at the measurement locations. Velocity measurements were taken using LDV in the x, y, and z directions to verify the type of mode traveling in the input fibers, and only the measurements from the L01 mode in the x direction were used. As shown in Figure 2.2(b), the velocity measurements were taken at four locations along the input fibers to find the average amplitude and the velocity of the mode. Each location was 2 cm apart, starting from the end of the adhesive bond. The measurement locations were spray coated with white powder (weld check spray) so that the laser emitted from

the LDV could better reflect from the surface and thus acquire more accurate measurements. For each measurement, the sampling frequency of 6.25 MHz was used and averaged over 1000 samples.

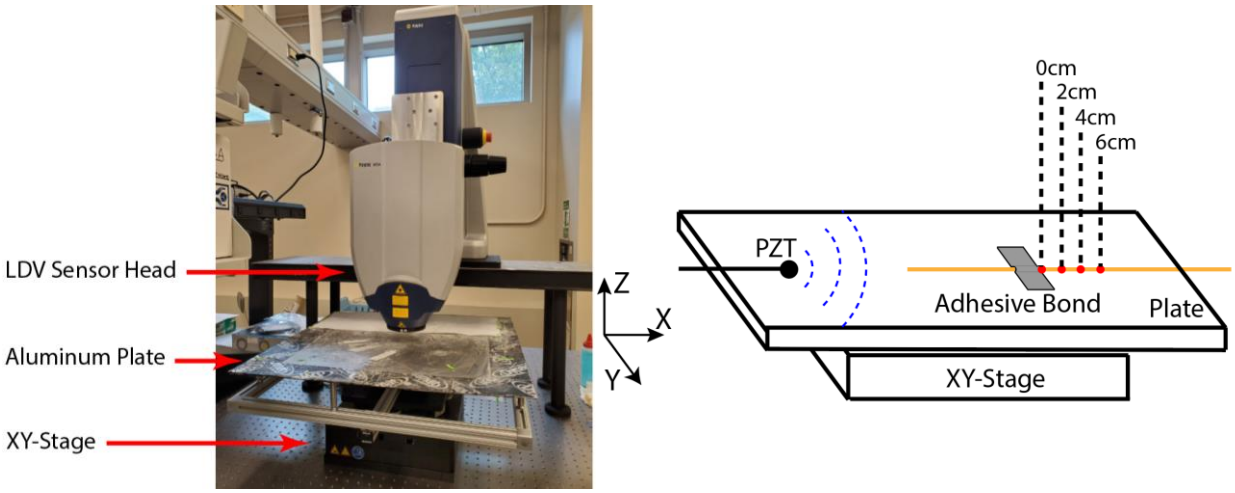

(a) (b)

Figure 2.2 (a) Laser Doppler Vibrometer setup. (b) Four LDV measurement points at location 1 from Figure 2.1.

The output L_{01} mode was measured with an FBG sensor at location 2, shown in Figure 2.1, using the edge filtering technique. The output wavelength of the tunable laser was set to the midpoint of the FBG ascending edge of the reflected spectrum. The L_{01} mode was measured through the optical power modulations at the photodetector due to the strain induced wavelength shift in the FBG [6]. The acoustic coupler did not affect the optical lightwaves through the output optical fiber.

To fabricate the acoustic couplers, a custom metal mold was designed [23]. The mold was designed large enough to create a coupler with a 600 µm diameter fiber. Note that the intention was to fabricate a repeatable, short length acoustic coupler, not to optimize the coupler geometry.

Figure 2.3 shows a dimensioned drawing and photograph of the custom mold. Rexco Coverall Film and LPS Dry Film were pre-applied to the molding surface so that the coupler could be easily released from the mold. The two fibers were laid down on the groove of the mold shown in Figure 2.3(b). Then, two upper presses were placed on either side of the mold to hold down the fibers. Lastly, the CA adhesive was applied on the location identified in Figure 2.3(b), and the upper press was placed to mold the shape of the coupler. The length of the coupler is 3.175 mm, and the curing time was 3 hours. Figure 2.3(d) shows an image of one of the couplers (a 125 μm diameter fiber coupled to a 600 μm diameter fiber), which is combined from multiple 500× microscope images. This particular input-output fiber combination had the largest diameter mismatch.

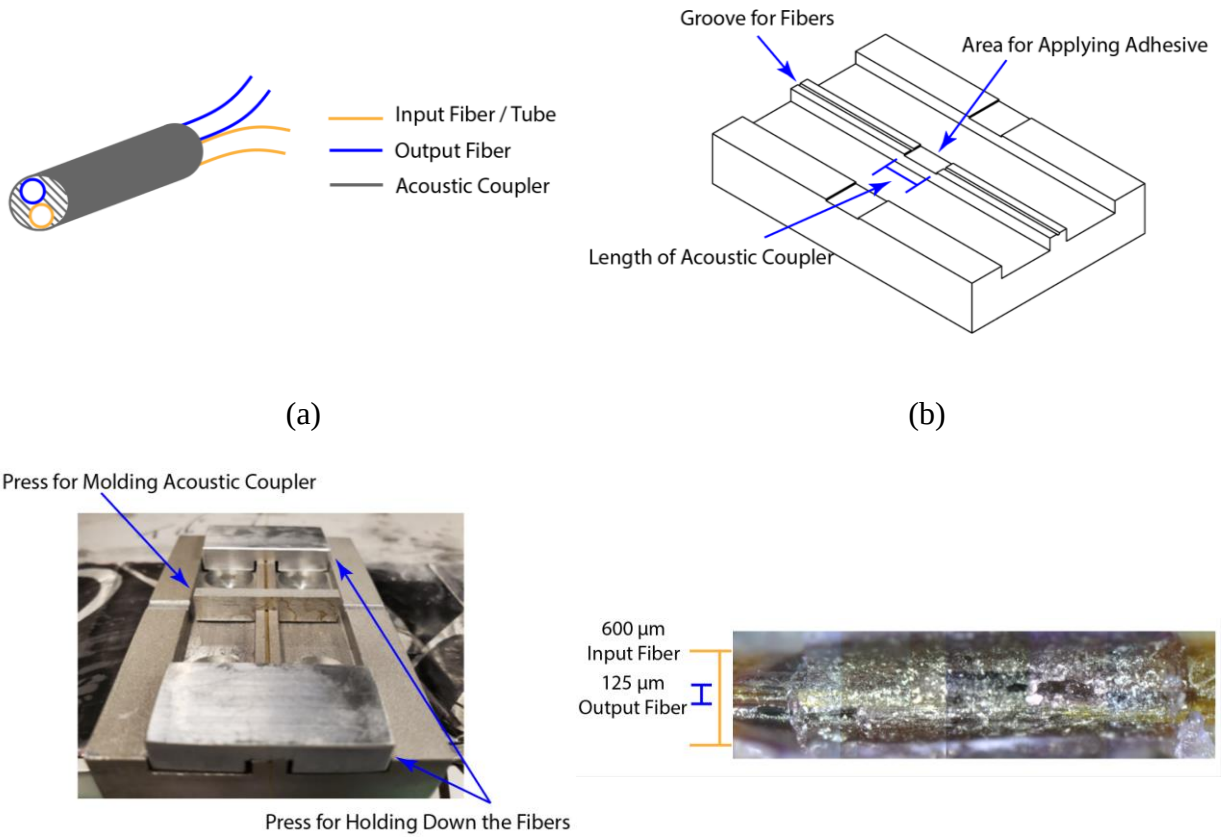

Figure 2.3 (a) Drawing of the coupler, (b) computer-aided design (CAD) drawing of the metal mod, (c) picture of the metal mold used for creating the acoustic coupler, and (d) acoustic coupler with 125 µm output fiber coupled to 600 µm input fiber.

2.3 Acoustic Coupling Between Different Fiber Geometries

The first set of experiments measured the acoustic coupling between two silica fibers with different cross-sectional geometries. Solid fibers with different diameters and hollow capillary tubes with different inner and outer diameters were used as the input fiber, while a standard 125 µm silica optical fiber (with polyimide coating) was used for the output fiber. The solid fibers were optical fibers with a silica core and cladding, while the hollow core fibers had an air core and silica

cladding. Both fibers were coated with polyimide. The cross-sectional geometry and dimensions of the fibers used in the experiment are shown in Figure 2.4 and Tables 2.1 and 2.2. We first verify the wave velocity of the L_{01} mode in each fiber and then calculate the acoustic coupling efficiency between each fiber and the standard single-mode silica optical fiber.

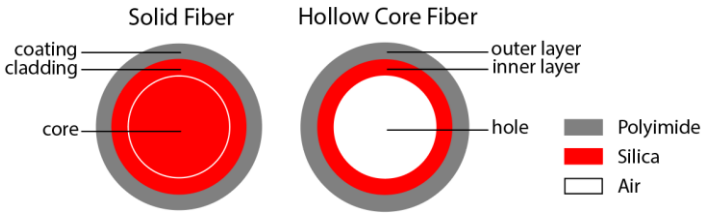

Figure 2.4 Cross-sectional geometry of input fibers

Table 2.1 Dimensions of the solid input fibers

Reference	125μm	200μm	300μm	400μm	600μm
Core diameter(μm)	9	200	300	400	600
Cladding diameter(μm)	125	220	330	440	660
Coating diameter(μm)	145	239	370	480	710

Table 2.2 Dimensions of the hollow core input fibers

Reference	30μm	75μm	150μm
Hole diameter(μm)	30	75	150
Cladding layer diameter(μm)	126	126	323
Coating layer diameter(μm)	150	150	363

Figure 2.5(a) shows the input signal to the PZT, which is a 5.5 cycle 300 kHz Hanning windowed function that was used for all measurements. Figures 2.5(b) and 2.5(c) plot the LDV velocity measurements of the L01 modes measured along the 600 μm solid fiber and 75 μm hollow

core fiber, respectively. For each figure, the four measurements correspond to the four locations indicated in Figure 2.2(b). The S_0 Lamb wave was successfully coupled to the L_{01} mode in the input fiber for both the solid and hollow core fibers. Additionally, the waveform of the mode was preserved. The amplitude of the L_{01} mode in the input fiber was calculated by averaging the peak-to-peak amplitude of the wave packet at the four locations. The wave velocity of the L_{01} mode was found by cross correlating the input wave packet with the measured wave packet at the four different locations and averaging the four values. The resulting time of arrival is represented by the red dotted line in Figure 2.5. The second wave packet, measured at around 0.09 ms at the adhesive bond (0 cm), is the L_{01} mode coupled from the A_0 mode. The LDV also captured the y- and z-direction velocity measurements of the F_{11} mode generated in the input fiber, but the F_{11} mode attenuates rapidly and is not detected by the FBG so it will not be discussed here.

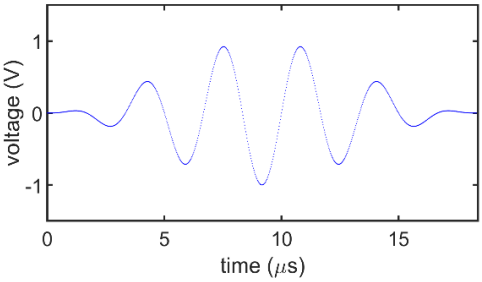

(a)

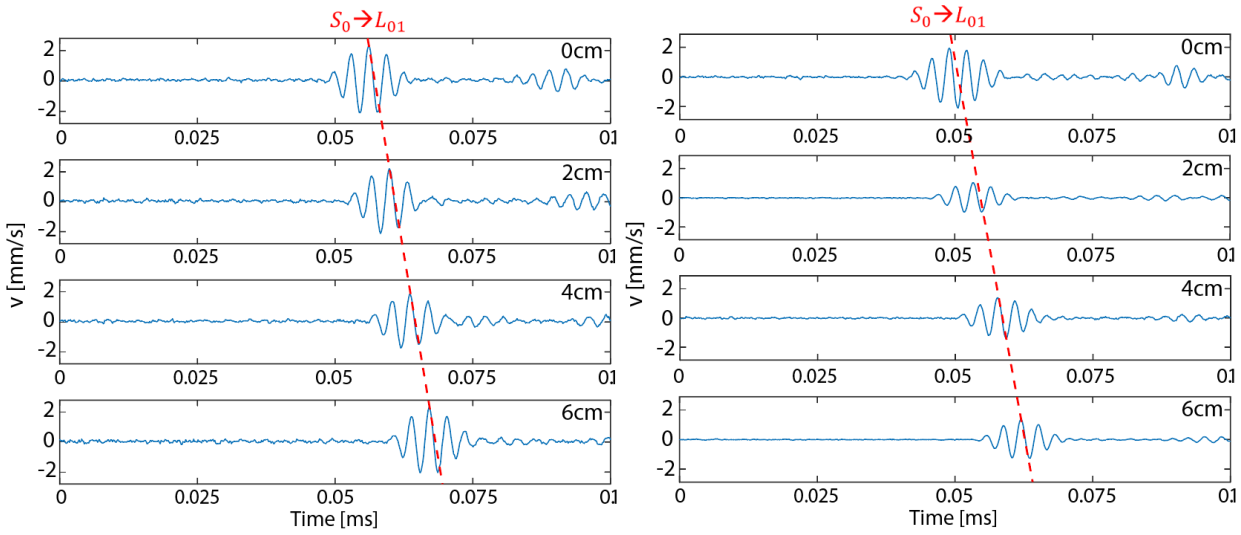

(b) (c)

Figure 2.5 (a) Input 5.5 cycle Hanning windowed function. L01 mode measurements of the input fiber for (b) 600 µm solid fiber and (c) 75 µm hollow core fiber. Red dashed line shows the arrival time from the L01 velocity calculation.

The theoretical velocity of the L01 mode for each solid fiber diameter was also calculated using the elastic wave model in thin rods with multiple layers [24]. The phase velocity of the lowest longitudinal mode is

$$v_{phase} = \left\{\frac{[E_1 a^2 + E_2(b^2 - a^2)]}{[\rho_1 a^2 + \rho_2(b^2 - a^2)]}\right\}^{\frac{1}{2}} \tag{2.1}$$

where subscript 1 is for silica, and 2 is for polyimide. *E* is Young's Modulus, *a* is the outer radius of the cladding, *b* is the outer radius of the coating, and ρ is the density. Equation (2.1) is based on the assumption that the fiber diameter is much smaller than the wavelength of the propagating L_{01} mode. Then, by using Rayleigh's formula, the group velocity is

$$v_{group} = v_{phase}\left(1 - \frac{\omega}{v_{phase}}\frac{dv_{phase}}{d\omega}\right)^{-1} \tag{2.2}$$

where ω is the angular frequency. The L_{01} mode is relatively non-dispersive over the range of operating frequencies we use; therefore, the group velocity is equal to the phase velocity [25].

Figure 2.6 compares the measured to the theoretical velocities for the solid fibers of different core diameters. The velocities of the L_{01} mode in solid fibers range from 5138.89 m/s for the 125 μm diameter fiber to 5441.64 m/s for the 600 μm diameter fiber. The measured and theoretical velocities plotted in Fig. 6 fibers are extremely close to each other.

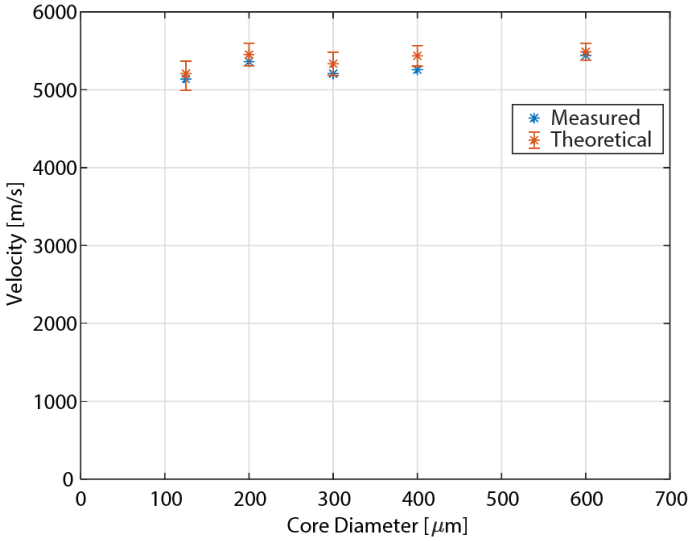

Figure 2.6 Comparison of measured velocities and theoretical velocities of L_{01} mode in solid fibers.

The theoretical velocity of the L_{01} mode for each hollow core fiber was predicted using the software package PCDisp [26]. Figure 2.7 compares the measured to the theoretical velocities for the hollow core fibers. The dimensional tolerance was larger for the hollow core fibers than the solid optical fibers; therefore, the uncertainty in the theoretical predictions was larger. The maximum and minimum velocities based on the dimensional tolerances are plotted as error bars in Figure 2.7. The theoretical velocities are not as close to the measured velocities as for the solid fibers. Most likely this is due to the uncertainties in the material properties for the hollow fibers, which were not specified by the manufacturer. However, the trend of the two data sets is the same.

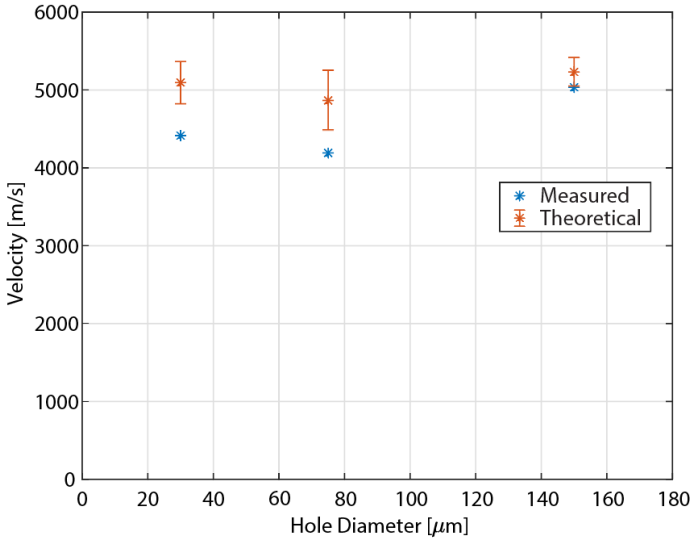

Figure 2.7 Comparison of measured velocities and theoretical velocities of L_{01} mode in hollow core fibers.

Next, the amplitude of the L_{01} mode coupled to the output fiber through the acoustic coupler was measured using the FBG on the output fiber. The wave amplitudes from the LDV are measured as the local axial velocity of the optical fiber, and the wave amplitudes from the FBG are measured in axial strain. In order to compare the two measurements, the strain amplitude at the FBG was converted to axial velocity. The equation for the axial displacement u due to a single-frequency planar wave propagating in the axial direction in the optical fiber is

$$u = Asin(2\pi ft - x) \tag{2.3}$$

where x is the axial coordinate, f is the frequency of the wave, A is the amplitude of the wave, and t is time. The axial velocity can be expressed as

$$v = \frac{du}{dt} = A(2\pi f)\cos(2\pi f t - x) \tag{2.4}$$

The local axial strain at a point in the optical fiber is

$$\epsilon = \frac{du}{dx} = -A\cos(2\pi f t - x) \tag{2.5}$$

Combining Equations (2.4) and (2.5), the axial velocity can be related to the axial strain,

$$v = -2\pi f \epsilon \tag{2.6}$$

Since the frequency of the input wave was constant for the experiments, the axial velocity and the strain are simply related by a constant. Although the wave used in the experiments is a Hanning windowed function containing different frequencies, this derivation for a single-frequency wave provides a good approximation to directly compare the axial velocity and strain.

The ratio of the measured output fiber-to-input fiber amplitudes of the L_{01} mode measurements are plotted in Figure 2.8 for different input fibers. The data is normalized to the control case, in which both the input and output fibers are the 125 μm silica single-mode fiber. To compare the results for both the solid and hollow core optical fibers, the measurements are plotted as a function of the cross-sectional area of silica on the input fiber. The results were similar for both types of fiber as a function of the cross-sectional area. Interestingly, the amount of energy coupled to the output fiber was higher than that of the control case for all input fibers that were larger in the cross-sectional area than the output fiber.

It can be seen that the amplitude of the coupled L_{01} mode increased approximately linearly with the cross-sectional area, until it reached a maximum between the 300 and 400 μm diameter solid fibers (a cross-sectional area ratio of 2.4–3.2 for the input to output fibers). There is,

therefore, clearly an optimum diameter ratio to maximize the acoustic coupling. This optimum is not 1.0, as predicted by the coupled-mode theory. The decrease in coupling efficiency above the 300 μm diameter fiber may be due to the fabrication of the coupler using the adhesive bond. Once the fiber sizes are significantly mismatched, the adhesive geometry begins to be distorted. The data of Figure 2.8 demonstrates that the coupling behavior is more complex than described by the coupled-mode theory. However, the exact trends are likely strongly dependent on the coupler geometry and fabrication method. Therefore, future numerical simulations of the ultrasonic wave propagation from one waveguide to another through the adhesive coupler may be necessary to fully understand the behavior of Figure 2.8.

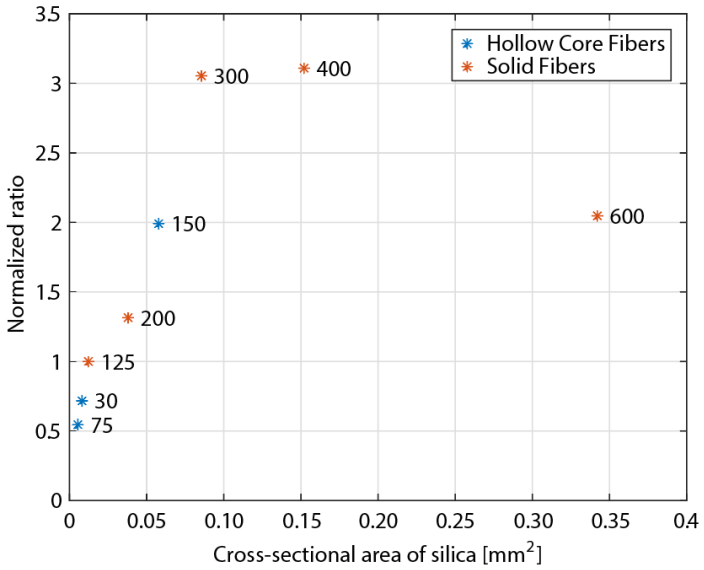

Figure 2.8 Normalized ratio of L_{01} mode coupling for solid and hollow core fibers, plotted as a function of cross-sectional area. Labels next to each data point are reference labels from Tables 2.1 and 2.2.

2.4 Acoustic Coupling Between Fibers of Different Material Properties

We next characterized the acoustic coupling efficiency between fibers with different material properties. We varied the material of uncoated, metal input waveguides for use as the input waveguide, while keeping the geometry and cross-sectional area approximately constant. The same output single-mode silica fiber was used as for the previous experiments. The material properties for input waveguides and output fiber (ignoring the polyimide coating) are shown in Table 2.3. $\sqrt{E/\rho}$ represents the theoretical wave velocity in the metal waveguides derived from Equation (2.1). The experimental setup, shown in Figure 2.9, is identical to the previous experiment, except metal waveguides are used as the input fiber.

Table 2.3 Mechanical properties of metal waveguide

	Input Waveguide			**Output Fiber**
Material	**Aluminum**	**Copper**	**Steel**	**Silica**
Cross-sectional area [mm^2]	0.6362	0.6362	0.4185	0.0123
E [GPa]	69	117	210	72.5
P [kg/m^3]	2710	8940	9030	2650
$\sqrt{E/\rho}$ [m/s]	5046	3618	5108	5231

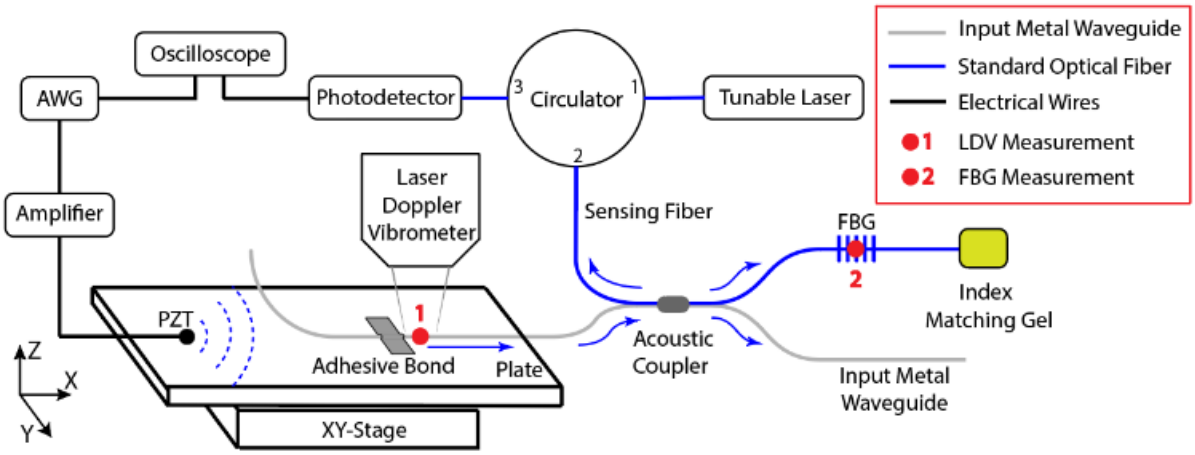

Figure 2.9 Setup of the metal waveguide experiment, with acoustic wave paths shown as blue arrows and measurement location shown as red dot.

Figure 2.10 shows the L_{01} mode measurement on the output fiber collected using the FBG sensor. The top plot of Figure 2.10 shows the measurement when the aluminum wire was used as the input waveguide, the middle plot when copper wire was used, and the bottom plot when steel wire was used. Note that due to the wave velocity difference specified in Table 2.3, the theoretically predicted arrival time of the L_{01} mode is 155 μs for the aluminum, 195 μs for the copper, and 155 μs for the steel input waveguides. These theoretical velocities match well to the experiments. The L_{01} mode measurement was collected on the input metal waveguide using the LDV. The LDV measurement was collected 10 times for each metal wire case, and the average was calculated. The ratio of the output fiber to input waveguide amplitudes of the L_{01} mode measurements is plotted in Figure 2.11 for each input waveguide and normalized to the same value as the data of Figure 2.8.

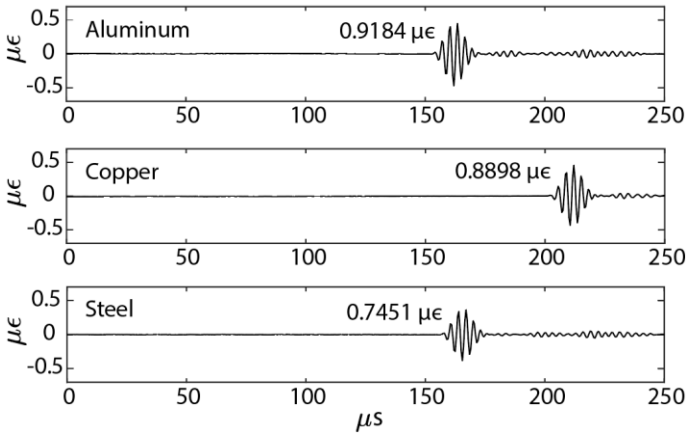

Figure 2.10 L_{01} mode measurement on output fiber using FBG when aluminum, copper, and steel wire were used as input waveguides.

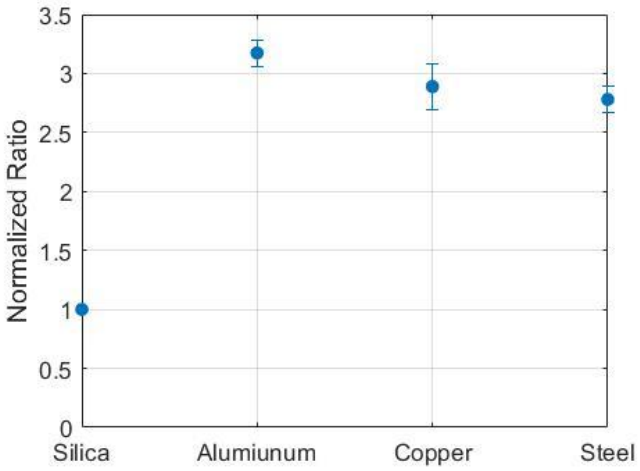

Figure 2.11 Normalized ratio of L_{01} mode transfer with respect to input waveguide material. Error bars show one standard deviation between measurements.

We can observe from Figure 2.11 that the coupling from the input metallic wires to the silica optical fibers was comparable to that of the best cases from Figure 2.8. Some of this strong coupling may be due to the fact that the attenuation in the metallic waveguides is lower than that of the polyimide coated optical fiber. Therefore, the wave does not attenuate as much in between the LDV measurement location and the actual coupler, creating an apparent increase in the

coupling efficiency. It is therefore difficult to compare the results to those of Figure 2.8, as the exact difference in attenuation coefficients is not known; however, we can compare the results between the three metallic waveguides. The ratio of the transferred wave is greatest when the aluminum input waveguide is used and smallest when steel input waveguide is used. From Table 2.3, we see that the modulus *E* for aluminum is closest to that for silica. The modulus *E* for steel has the greatest mismatch with that of silica among the three cases. The fibers of copper and aluminum have the same cross-sectional area but different coupling efficiencies; therefore, the fiber cross section is not the only critical parameter to the coupling efficiency. Additionally, the aluminum and steel fibers have close values of acoustic wavespeed ($\sqrt{E/\rho}$); however, their coupling efficiency does not scale with the cross-sectional area. Therefore, the coupling efficiency clearly depends on the relative modulus of elasticity between the waveguides, but in some unknown combination with other factors such as cross-sectional area or density.

2.5 Conclusions

The experimental results in this paper demonstrate that coupling two fibers through an adhesive bond permit the coupling of acoustic waves between them. While the coupling may not be as high of a performance as for fused fiber couplers, this technique allows the rapid connection of fibers to optical fibers containing sensors for field applications. In particular, these results demonstrate that the two fibers do not have to be the same to achieve good coupling efficiency. A range of different fiber sizes, geometries, and materials were demonstrated to sufficiently couple acoustic waves to a standard polyimide coated silica optical fiber. Therefore, the fiber that actually is used to collect the acoustic wave does not have to be an optical fiber. This feature increases the potential applications of using remotely bonded fabric reading centers in environments not suitable for silica. Unlike the solid fibers, the hollow core fibers could also be filled with other things such

as liquid or gas, which can change the physical properties of the input fiber and potentially allow us to tune the signal coupling. While different fiber diameters, geometries, and materials were demonstrated for coupling in this paper, there is still a significant amount of work that can be done to optimize the coupling behavior for particular applications. In addition, numerical analyses of the acoustic coupling through this adhesive bond could greatly aid this optimization process.

2.6 Acknowledgement

The authors thank the Office of naval Research (ONR) (N00014-19-1-2053) for the financial support of this research.

Chapter 3

Demonstration of Coherent Interference between Acoustic Waves Using a Fiber Ring Resonator

Optical fibers were previously demonstrated to propagate and detect acoustic modes that were converted from Lamb waves for structural health-monitoring applications; typically, a fiber Bragg grating sensor in the optical fiber is used to detect acoustic modes. Acoustic modes can transfer from one fiber to another through a simple adhesive bond coupler, preserving the waveform of the acoustic mode. This paper experimentally investigates the coherence of acoustic waves through the adhesive coupler, using a fiber ring resonator (FRR) configuration. This configuration was chosen because the wave coupled to the second fiber interferes with the original wave after it encircles the fiber ring. We performed this experiment using different geometries of optical fibers in the ring, including a standard single-mode optical fiber, a hollow silica capillary tube, and a large-diameter multi-mode fiber. The results demonstrate that the acoustic wave, when transferring through an adhesive coupler, interferes coherently even when the main and ring fibers are of different types. Finally, we demonstrate that the FRR can be applied for sensing applications by measuring the mode attenuations in the ring due to a changing external environment (water-level sensing) and measuring the optical-path length change in the ring (temperature sensing).

3.1 Introduction

Optical fiber sensors are commonly applied to collecting guided waves in structural health-monitoring systems. Recent papers have used fiber Bragg grating (FBG) sensors in a remote-bonding configuration to capture the guided wave [21,27,28]. In this case, the FBG sensor is not in direct contact with the structure, as shown in Figure 3.1. Instead, the fundamental symmetric (S_0) and antisymmetric (A_0) Lamb waves in a structure are converted to propagating fundamental

longitudinal (L_{01}) and flexural (F_{11}) waves in the optical fiber, through an adhesive bond, and are measured with a sensor at a remote location further along the fiber [10,11]. The use of a remote bonding configuration has been shown to increase the sensitivity of the FBG to small-amplitude guided waves [10].

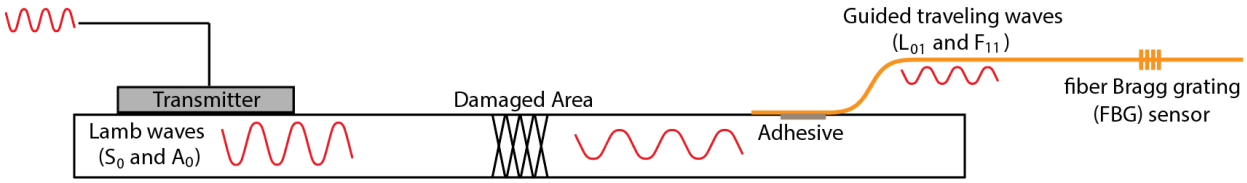

Figure 3.1 Remote bonding of a fiber Bragg grating sensor structure for guided wave inspection.

For structural health monitoring applications, it may also be beneficial to capture acoustic waves with different fibers and collect them into a single fiber for processing, or to split the wave from a single fiber into multiple fibers. Early papers demonstrated that these traveling ultrasonic waves can be coupled from one fiber to another through a standard fusion-spliced optical coupler [12,29]. However, fusion-spliced couplers require a precision manufacturing process due to the small wavelength of the light wave (in the order of a single micrometer) and the need to overlap the propagating mode fields between the fibers. These mode fields are confined near their cores; therefore, the fiber diameters need to be reduced in the coupler section. For field applications, adding an optical fiber to an existing sensor network that is bonded to the structure may require removing the existing fiber, then cleaving and splicing it to the coupler leads.

However, in cases where only acoustic coupling between the two fibers is required (and not optical coupling), the authors demonstrated a simpler technique, based on adhesively bonded couplers [19]. The wavelength of the L01 mode in a standard optical fiber at ultrasonic frequencies is in the order of a single centimeter; the longitudinal mode is, thus, much more widely distributed

in the cross-section of the optical fiber. Therefore, the same precision is not required in the coupler dimensions and the fiber diameter does not need to be reduced. Similarly, Leal et al. [19] demonstrated a fiber-optic acoustic splitter by attaching a segment of optical fiber at two points of another main optical fiber using an adhesive. Using adhesive bonds to couple acoustic waves allows the rapid coupling of the fibers and the extension of new sensors to an already installed sensing system. Since the fibers do not have to be fused, different types and diameters of fibers can also be coupled, meaning that the sensor fiber does not have to be a standard single-mode fiber [30]. Kim et al. [30] demonstrated acoustic-wave transfer via a cyanoacrylate adhesive bond coupler between a polyimide-coated, single-mode optical fiber and different fiber types. These included a single-mode optical fiber, multi-mode optical fibers with different diameters, polyimide-coated silica capillary tubes, and metal fibers. The results published by Kim et al. [30] verified that the waveform of the L01 mode is preserved through the adhesive bond coupler and showed that the amplitude of the coupled mode is more complex than that described by the coupled-mode theory. However, the degree of coherence between the original and coupled acoustic waves after the adhesive bond coupler was used was not investigated.

Many optical fiber sensor multiplexing strategies rely on a high degree of signal coherence, including time division and frequency division multiplexing [31,32]. Therefore, to combine the signals from different collection points, it is important that the coherence of the acoustic waves should also be preserved after passing through the coupler. Acoustic waves retain their coherence as they propagate through a structure; therefore, correlating input signals transmitted from different locations with multiplexed signal measurements can be used to extract the contribution of specific sensors individually [33]. The degree of coherence of the ultrasonic waves themselves can also provide input about the integrity of the structure and the presence of scattering due to defects [34].

For this reason, coherence-based multiplexing uses low-coherence input waves to identify the source of each wave [35–37].

This paper experimentally investigates the coherence of acoustic waves through the adhesive coupler, using a fiber ring resonator (FRR) configuration. This configuration was chosen because the wave coupled to the second fiber interferes with the original wave after it encircles the fiber ring [38–41]. In addition, the FRR configuration allows us to estimate the coupling coefficient and coupling loss of the adhesively bonded coupler. We performed this experiment using several different geometries of optical fibers in the ring, including a standard single-mode optical fiber, a hollow silica capillary tube, and a large diameter multi-mode fiber. Finally, we demonstrate that the FRR can be applied for sensing applications by measuring the mode attenuation in the ring due to a changing external environment (water-level sensing) and measuring an optical path-length change in the ring (temperature sensing).

3.2 Materials and Methods

The experimental setup for testing acoustic FRR is shown in Figure 3.2a. A standard 125-μm diameter single-mode silica fiber with a polyimide coating was used as the main fiber (Micron Optics os1100, Atlanta, GA, USA). The main fiber had FBG sensors on each side of the fiber ring to measure the amplitude of the acoustic modes. FBGs 1 and 2 were 10 mm long and had Bragg wavelengths of 1584 nm and 1616 nm, respectively. One end of the main fiber was connected to the tunable laser (NetTest 3642 HE CL, Peabody, MA, USA) and photodetector (New Focus 1544, Milpitas, CA, USA) via a circulator. The output response from each FBG to the L_{01} acoustic mode was measured by tuning the tunable laser output to the rising edge of the FBG spectrum and then measuring the change in amplitude of the reflected signal. The edge filter was tuned, then the rising-edge slope was calibrated for each FBG, prior to every experiment.

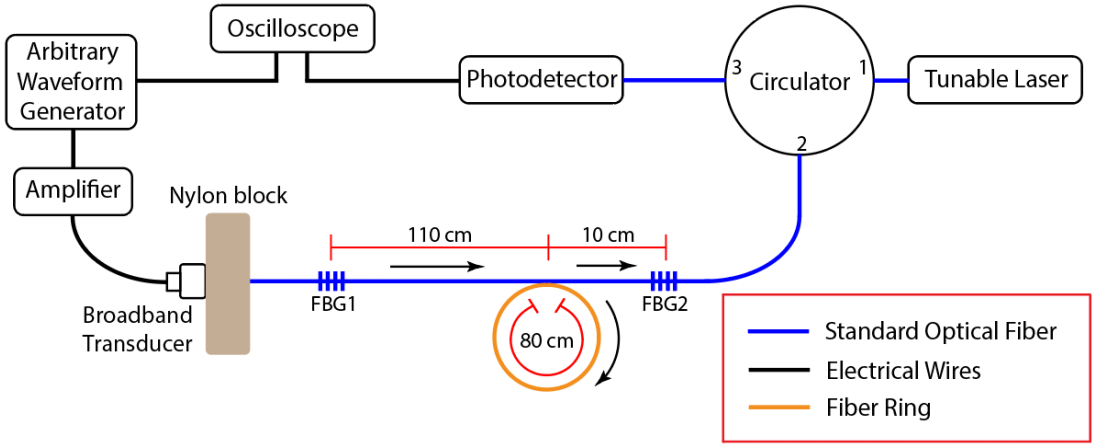

(a)

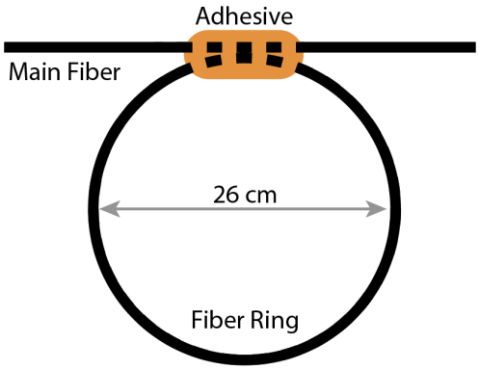

(b)

Figure 3.2 (a) Setup of the fiber ring resonator experiment, with acoustic wave paths shown as arrows. (b) Sketch of the fiber ring, attached to the main fiber using adhesive.

The FRR ring was fabricated by cleaving two ends of a fiber and splicing them into a ring shape. Then, the FRR ring was adhesively bonded to the main fiber, as shown in Figure 3.2(b). To ensure consistency of the adhesive quality, the main fiber and FRR were positioned and taped down to a metal surface, such that a few millimeters in the length of each fiber would align and be in contact with one other, then a single droplet of cyanoacrylate adhesive (Loctite Ultragel Control) was applied to the region of contact.

The acoustic wave coherence was investigated in terms of the fiber ring resonator for three different ring fibers: a standard 125 μm-diameter single-mode fiber with a polyimide coating, a 220 μm-diameter multimode silica fiber with a polyimide coating, and a 126 μm-diameter silica capillary tube with a 75 μm-diameter hole and polyimide coating. The standard single-mode fiber was selected to examine the wave transfer between identical fibers, while the other two fibers were selected to examine the wave transfer from the single-mode fiber to a fiber with different cross-sectional geometry.

Sinusoidal, ultrasonic L_{01} modes were launched into the main optical fiber, using a broadband transducer (Olympus C407, Waltham, MA, USA) with varying excitation frequencies from 700 kHz to 730 kHz. Different numbers of cycles were excited (from 1 to 200), depending on the experiment. The burst period for the waveform generator was set to 10 ms, to avoid any possible interference with the reflection of the preceding excitation. The transducer was attached to a nylon block, then one end of the main fiber was glued into a hole that was punctured into the opposite surface of the nylon block. The input excitation signals from the arbitrary waveform generator (AWG) were time-synchronized with the measurement acquisition by sending a TTL trigger signal to the oscilloscope (Agilent Technologies DSO5032A, Santa Clara, CA, USA).

3.3 Results

3.3.1 Investigating Acoustic Wave Coherence Using the FRR

The behavior of the acoustic FRR was analyzed using the Sagnac-effect-based resonant fiber optic gyro model derived by Ying et al. [42] for an optical system. This formulation was chosen for our analysis of the passing of acoustic waves through the adhesive bond because it includes a coupling loss coefficient for the coupler. For fused optical couplers, this loss might be

negligible; for the adhesively bonded coupler, it is expected to be significant. Figure 3.3 shows the acoustic wave pathways through the FRR.

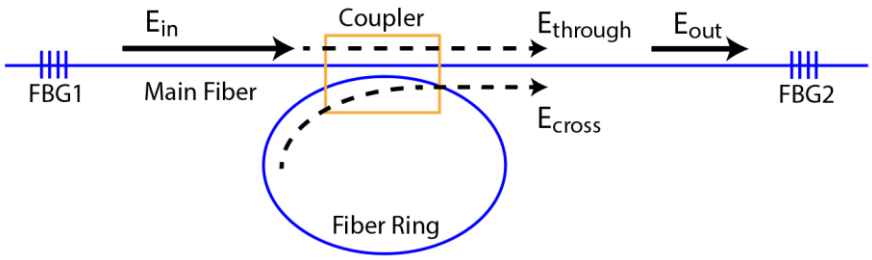

Figure 3.3 Schematic of the wave flow in FRR for a standard single-mode fiber ring.

The input wave to the system, E_{in}, is measured with FBG 1. In the model of Ying et al. [42], the input wave amplitude is defined as a function of time:

$$E_{\text{in}}(t) = E_0 e^{\left[2\pi i\left(f_0+\frac{kt}{2}\right)t\right]} e^{(i\psi_0)} \tag{3.1}$$

where E_0 is the amplitude of the wave, f_0 is the input frequency, k is the frequency sweep rate of the wave and ψ_0 is the initial phase of the wave. The wave then reaches the FRR and a portion passes directly through the main optical fiber without going through the FRR, $E_{through}$:

$$E_{\text{through}}(t) = E_0 e^{\left[2\pi i\left(f_0+\frac{kt}{2}\right)t\right]} e^{(i\psi_0)} \times (1-k_c)^{\frac{1}{2}}(1-a_c)^{\frac{1}{2}} \tag{3.2}$$

where k_C is the coupling coefficient of the coupler and a_C is the coupling loss coefficient. These two coefficients are defined as the fraction of the intensity of the wave, either coupled or dissipated, which is why Equation (3.2) includes the square root of these terms. The portion of the wave entering the fiber ring is expressed as:

$$E_{\text{ring}}(t) = E_0 e^{\left[2\pi i\left(f_0+\frac{kt}{2}\right)t\right]} e^{(i\psi_0)} \times (k_c)^{\frac{1}{2}}(1-a_c)^{\frac{1}{2}} \tag{3.3}$$

and the remaining portion is dissipated through the coupler loss. The wave E_{ring} circles the FRR, and a portion is recoupled into the main optical fiber.

The portion remaining in the FRR circles the FRR through multiple passes, each time coupling a portion of the wave into the main fiber, until the amplitude of the wave is negligible. Each time the wave propagates through the ring it is attenuated, due to the propagation loss per unit length in the fiber ring, a_L, and is phase-shifted due to the optical path length of the ring. The value for a_L in a standard, polyimide-coated single-mode optical fiber for the L mode at 300 kHz was measured by Wee et al. [10] to be 0.19 m^{-1} . The sum of the waves exiting the FRR with each pass is labeled as E_{cross}. After the Nth pass through the fiber ring, the resulting E_{cross} is expressed as:

$$\begin{aligned} E_{\text{cross}}(t) = {} & E_0 k_c (1-a_c)(1-a_L)^{\frac{1}{2}} e^{\left[2\pi i\left(f_0+\frac{kt}{2}\right)t\right]} e^{(i\psi_0)} e^{(i\pi)} \\ & \times \sum_{n=1}^{N} \left[(1-k_c)^{\frac{1}{2}}(1-a_c)^{\frac{1}{2}}(1-a_L)^{\frac{1}{2}}\right]^{n-1} \times e^{\left[-2\pi i\left(f_0 n\tau + kn\tau t - \frac{kn^2\tau^2}{2}\right)\right]} \end{aligned} \tag{3.4}$$

The transit time is calculated as $\tau = c_0 L$, where c_0 is the velocity of the acoustic mode in the ring fiber and L is the length of the ring. The velocity of the acoustic mode in each fiber type was previously measured experimentally using laser Doppler vibrometry by the current authors [30]. The output wave amplitude after the FRR is the total of these two contributions, expressed as:

$$E_{\text{out}}(t) = E_{\text{through}}(t) + E_{\text{cross}}(t) \tag{3.5}$$

Initial experiments were performed with standard single-mode fiber as the ring and a 700 kHz and 702 kHz excitation signal. Figures 3.4(a)–(f) show the recorded signals at FBG1 and FBG2 for these experiments. Figure 3.4(a) shows E_{in}, measured by FBG1 for 1 cycle of the sine-wave input. At around 60 μs, we observed the input sine wave, and after approximately 10 μs we observed a second sine wave, which is a reflection that is possibly caused by the wave traversing through the nylon block. Figure 3.4(b) shows the FBG2 reading for the same excitation, with the waves $E_{through}$ and E_{cross} after the first pass through the ring, and E_{cross} after the second pass through the ring. The theoretical arrival time for each signal is marked in Figure 3.4(b), confirming the identification of each wave. As the velocities of the acoustic modes are much slower than the optical light waves in optical fibers, the separation time is visible in the measurements and is much larger than the burst duration. Therefore, no interference occurs between $E_{through}$ and the multiple E_{cross}. In addition, we can see the actual waveform in the signals. However, from this experiment, we observed that the amplitude of E_{cross} after the second pass through the ring is small compared to the other wave packets; therefore, we only considered E_{cross} after the first pass in the subsequent experiments. This rapid decay is due to the loss in the coupler and the propagating loss in the fiber ring, which are both significant for these experiments.

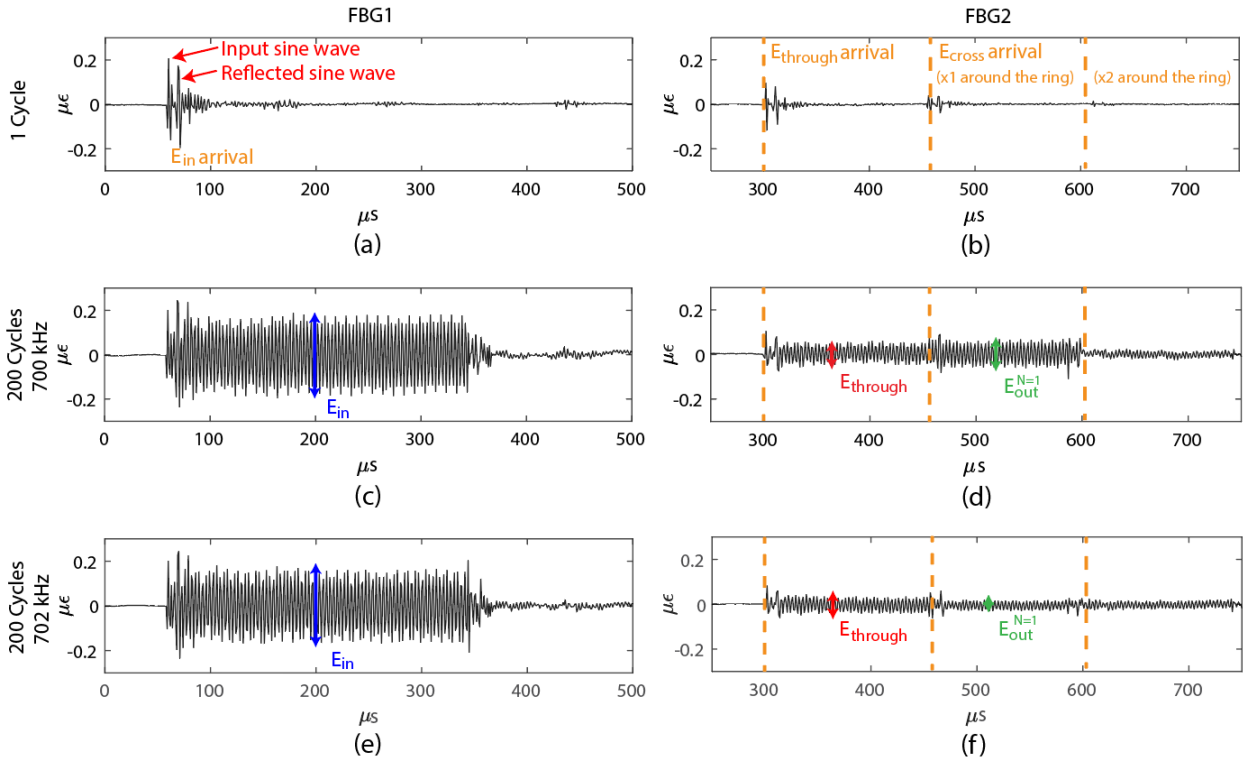

Figure 3.4 (a) FBG1 measurement for 1 cycle per burst, (b) FBG2 measurement for 1 cycle per burst, (c) FBG1 measurement for 200 cycles per burst at 700 kHz, (d) FBG2 measurement for 200 cycles per burst at 700 kHz, (e) FBG1 measurement for 200 cycles per burst at 702 kHz, and (f) FBG2 measurement for 200 cycles per burst at 702 kHz.

Figure 3.4(c) shows the input wave to the FRR, as measured by FBG1, when the number of cycles per burst is increased to 200, thus increasing the duration of the wave packet to approximately 300 μs. The double sine wave input seen in Figure 3.4(a) is repeated as the number of cycles of the sine wave is increased, as seen in Figure 3.4(c)-(f). Although not as ideal as a sinusoidal wave, the periodic form allows the wave packets to interfere. The amplitude of the input signal E_{in} is shown in Figure 3.4(c). Since the duration of E_{in} was increased, the wave packet of $E_{through}$ partially overlapped and interfered with the wave packet of E_{cross}. In Figure 3.4(d), the amplitude of $E_{through}$ and the amplitude of the signal when E_{out} represents the interference outcome

of $E_{through}$ and E_{cross} are shown. To demonstrate that interference is actually occurring, the frequency of the input wave was changed slightly. Figures 3.4(e), (f) show the same FBG1 and FBG2 measurements but, at 702 kHz, there is an input excitation. In Figure 3.4(d) we can observe constructive interference as $E_{through}$ overlaps with E_{cross} and, in Figure 3.4(f), we can observe the destructive interference.

We next used the theoretical model to estimate the coupling coefficient and coupling loss coefficient for the coupler. From Figure 3.4(b), we can observe that the amplitude of the wave decreases significantly when N is greater than 2; thus, we only theoretically model the wave interference of the acoustic FRR for N = 1. Since each measurement is taken at a fixed frequency, the sweep rate, k, is zero and the input wave equation becomes:

$$E_{\text{in}}(t) = E_0 e^{[2\pi i f_0 t]} e^{(i\psi_0)} \tag{3.6}$$

Setting N = 1, we find the power ratio of the output and input wave,

$$\left|\frac{\mathrm{E}_{\text{out}}^{N=1}}{E_{in}}\right|^2 = \left|(1-k_C)^{1/2}(1-a_C)^{1/2} - k_c(1-a_C)(1-a_L)^{1/2}\mathrm{e}^{-2\pi i f_0 L/c_0}\right|^2 \tag{3.7}$$

where the only unknown parameters are k_c and a_c. Therefore, we can use the measurements at two different frequencies to fit the values of k_c and a_c. Since the full waveform can be measured, in contrast to optical measurements, we do not need to average the amplitude ratio over time; instead, we can determine the amplitude directly from the waveform.

Figures 3.5(a) and (b) plot the peak-to-peak amplitude measurements of E_{in}, $E_{through}$, and E_{out} N=1 as a function of the input frequency f_0 . Figure 3.5(a) shows the result for the 75 μm

hollow-core fiber, while Figure 3.5(b) shows the result for the standard 125-μm single-mode solid fiber. Between the two experiments, the ring was removed, and the standard single-mode fiber ring was attached to the main optical fiber. Therefore, the coupling to the broadband transducer and E_{in} remained the same. The amplitude of E_{in} varied with frequency because the output amplitude from the broadband transducer varied; the wave coupling can vary with the frequency at the transducer to the nylon block interface and at the nylon block to the main fiber interface. Based on these data sets, we examined the wave interference pattern, as shown in Figures 3.5(c) and (d) in which the E_{out} N=1 interference pattern is normalized with E_{in}.

The results in Figures 3.5(c) and (d) resemble the frequency response of an optical interferometer. In fact, the free spectral range can be calculated using the exponential term in Equation (3.7), in which the frequency values that satisfy the condition $f_0 L/c_0 = n$ for all positive n integers mark the locations of the peaks. Using the length of the FRR and the velocity of the L_{01} mode, the free spectral range of the 75-μm hollow-core fiber ring is 5.1 kHz, while the free spectral range of the standard single-mode fiber ring is 6.5 kHz, which is consistent with the experimentally measured data in Figures 3.5(c), (d). Therefore, the wave before and after the coupler interfered coherently.

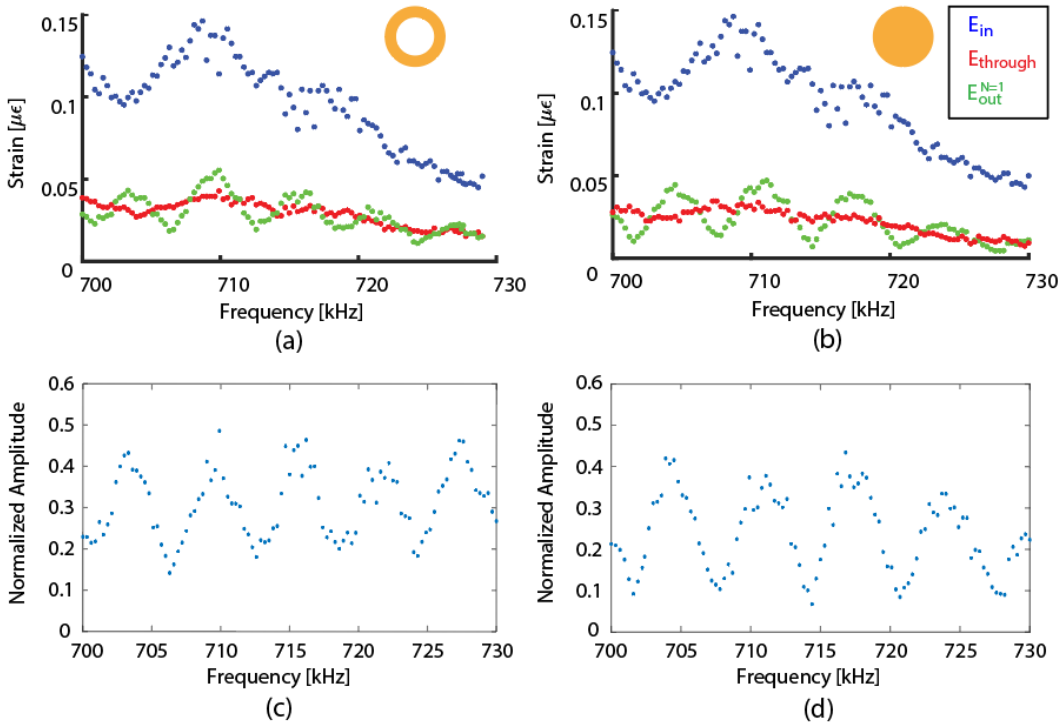

Figure 3.5 Wave interference pattern from 700 kHz to 730 kHz for: (a) a 75-μm hollow-core fiber ring and (b) a standard single-mode fiber ring, and normalized wave interference pattern from 700 kHz to 730 kHz for (c) a 75-μm hollow-core fiber ring and (d) a standard single-mode fiber ring.

We next fitted the data from the measurements at the two frequencies into Equation (3.7), to find the k_C and a_C for each fiber type. The results are shown in Table 3.1. The coupling coefficient, k_c, varied from approximately 0.6 to 0.8 and increased with the fiber silica cross-sectional area of the ring fiber. This behavior was consistent with the previous experiments by Kim et al. [30]. The coupling loss, a_C, was significant for all cases, as expected. In particular, the value for the 220 μm solid fiber ring was much larger than in the other cases, which may be due to the significant fiber size mismatch between the two fibers. In addition, the ring fiber was bent into a circular configuration prior to bonding; therefore, the large-diameter fiber probably put more

stress on the adhesive bond. These results show that the property of the acoustic FRR system can be tuned, based on selecting different fiber ring geometries.

Table 3.1 Empirical k_C and a_C for a 75-μm hollow-core fiber ring, a standard single-mode fiber ring, and a 220-μm solid fiber ring.

75 μm hollow core fiber ring (8051 μm² silica)		**Standard single-mode fiber ring (12,271 μm² silica)**		**220 μm solid fiber ring (38,013 μm² silica)**	
k_C	a_C	k_C	a_C	k_C	a_C
0.5955	0.7430	0.7181	0.7939	0.8219	0.9494

3.3.2 Demonstration of Acoustic FRR as Sensors

Based on the experiments of the previous section, an FRR can easily be fabricated and attached to any existing sensing fiber using the adhesive coupler, to function as a separate sensor. To show the function of an FRR as a sensor, two demonstrations were performed. One demonstration measures the mode attenuation in a ring in response to a changing external environment, due to a changing water level, and one measures an optical path length change in the ring due to temperature. Note that these demonstrations were only conducted to show possible applications, and that they were not optimized for practice.

The first demonstration utilized the acoustic FRR as a water-depth sensor, based on the amplitude of the signal from the ring fiber. The acoustic wave in the waveguide attenuated faster when the external medium was water rather than air; so, depending on the amount of fiber ring being submerged in water, the interference pattern will change. For this demonstration, a standard single-mode fiber ring was used. The setup is identical to Figure 3.2; however, the fiber ring was put inside a water tank and the measurements were taken as the water level was incrementally

increased. The input wave was set at 703 kHz frequency, so that the interference pattern would be constructive.

Whereas the original coefficient of attenuation around the fiber ring was a_L, the attenuation coefficient is now expressed as:

$$a_L + \frac{L_w}{L}(a_w - a_L) \tag{3.8}$$

where L_w is the length of the fiber that is submerged in water. Figure 3.6 shows the measured $E_{out}^{N=1}$ interference pattern for water levels from 0% to 90%, along with an exponential curve fitted to the data. The output is normalized to $E_{through}$, so that the value of 1 corresponds to there being no energy remaining after the wave travels around the fiber ring. As the water level increased, the amplitude of E_{cross} reduced rapidly; thus, the amplitude ratio decreased, as expected. The sensor output was saturated when approximately 40% of the ring was submerged, confirming that the attenuation in water is considerably higher than that in air.

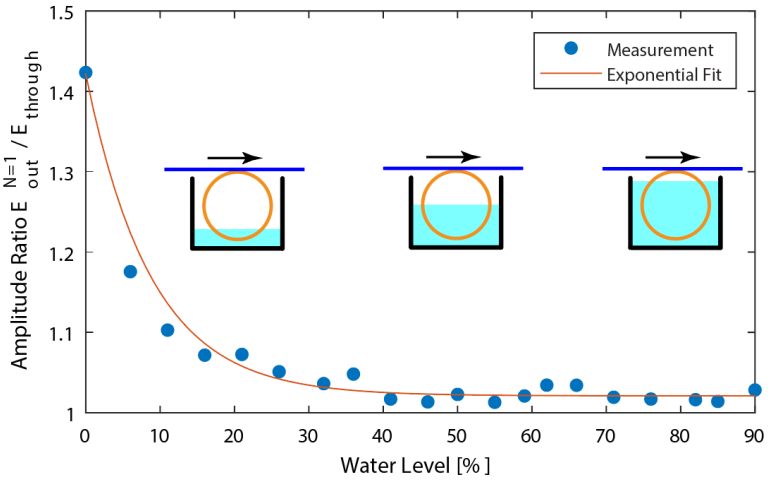

Figure 3.6 Normalized wave interference pattern for a standard single-mode fiber ring at water levels of 0% to 90%.

The second demonstration utilized the acoustic FRR as a temperature sensor, using the coherent interference of the acoustic wave. The standard single-mode fiber ring from Figure 3.2 was put inside an insulated container and the output amplitude was measured in a frequency range from 700 kHz to 715 kHz. Measurements were performed at three different temperatures: room temperature (21.0 °C), hot temperature (40.3 °C), and cold temperature (11.6 °C). First, the measurements were taken at room temperature, then the temperature was raised to the appropriate hot temperature by placing heat packs inside the container. The FRR was left in the container for 1 hour before taking measurements so that it could adjust to the hot temperature. After cooling the FRR back down, the measurements at room temperature were taken again; then, the temperature was lowered to the cold temperature by placing ice packs inside the container. The FRR was left in the container for 1 hour again, before taking measurements. The temperature inside the container was independently measured with a thermometer.

Figure 3.7 shows the frequency response measurements and their fitted curves. Figure 3.7(a) shows the frequency response for room temperature and the hot temperature, while Figure 3.7(b) shows the frequency response for room temperature and the cold temperature. In Figure 3.7(a), the measurement of the hot temperature is noisier than the other three measurements, due to the physical interference of the hot pack inside the container; the FBG was hanging in mid-air during measurements. A fast Fourier transform was performed on the four wave interference patterns to find the free spectral range, which was identical at 6.45 kHz. Using this information, sinusoidal curves were fitted to the frequency response, from which the peak frequency shift was found for each temperature change. The amplitude of the measurements drifted during the experiments, potentially due to changes in the support condition and the resulting contact with the coupler. However, the input frequencies for the peak locations were still the same between the

fitted curve and the measured curve. For the temperature change of +19.3 °C (from room temperature to the hot temperature) the peak frequency increased by 628 Hz and, for a temperature change of −9.4 °C (from room temperature to the cold temperature), the peak frequency decreased by 314 Hz. This result shows that the shift in the wave interference pattern is directly related to the change in the environmental temperature, and the calculated sensitivity value is 33.0 Hz/°C.

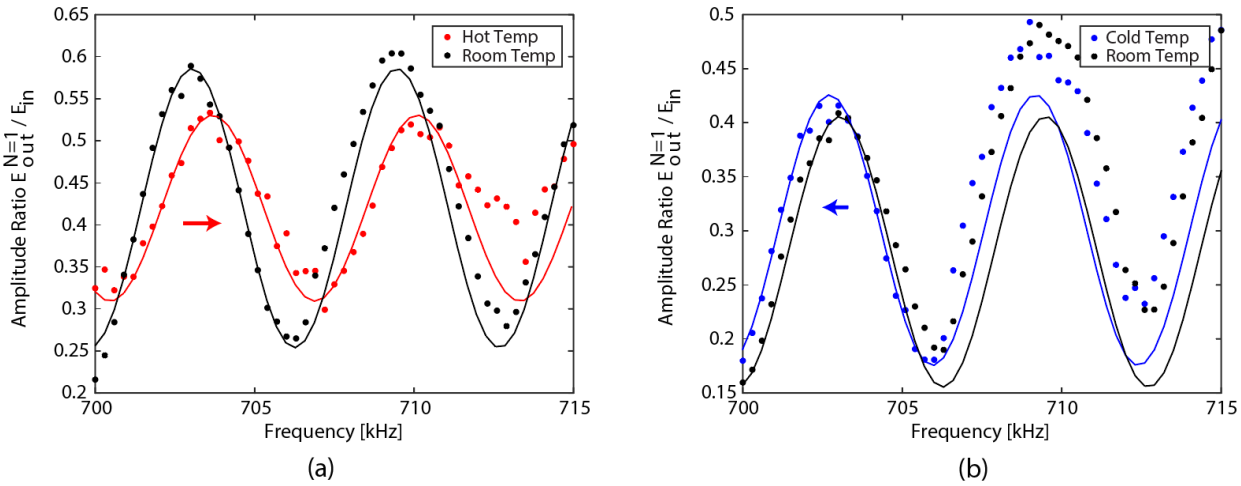

Figure 3.7 Wave interference pattern and fitted curves from 700 kHz to 715 kHz: (a) at room temperature and the hot temperature, and (b) at room temperature and the cold temperature.

3.4 Conclusions

The experimental results in this paper demonstrate that the acoustic waves transferring through an adhesive coupler interfere coherently. The degree of coherence was not estimated because the coupling loss was significant; however, the output of the FRR can be used for sensing applications that require interference in the input and output acoustic waves, as demonstrated with the temperature measurement experiment. Although the losses in the acoustic FRR, based on the adhesive bond coupler, are high, a unique feature is that the ring fiber used for measurement in the environment does not have to be a standard optical fiber. The ring fiber could be a different

material that reacts differently to the environment. Another possibility would be to fill the hollow-core fibers with liquids or gases, which allows even more opportunities for sensing applications. Although different fiber diameters and geometries were used as fiber rings in this paper, there is still a significant amount of work that should be conducted to further analyze and understand the geometrical properties that govern k_C and a_C, and how these can be varied to tune the output of the coupler and the FRR.

3.5 Acknowledgement

The authors thank the Office of naval Research (ONR) (N00014-19-1-2053) for the financial support of this research.

Chapter 4

FEA and ODE Analysis of Acoustic Coupling via Adhesive Coupler

In this study, we construct a finite element analysis (FEA) model of the adhesive acoustic coupler and validate with the previous experimental results. We also compare with the finite element simulations with an analytical model based on a set of ODEs describing the energy coupling between the two fibers and spring elements to represent the contact between the two fibers. COMSOL Multiphysics® software was used for the FEA because it is specialized in performing parametric sweeps. The finite element model reproduced the experimental results well, and so was used to investigate the behavior of the coupler as a function of different geometrical parameters for the coupler. We also demonstrate that the analytical model can describe the acoustic coupling behavior for adhesive bonded optical fibers, other than losses in the coupler due to the damping of the adhesive. The analytical model output is highly sensitive to the input conditions and the proper selection of these conditions needs further investigation.

4.1 Introduction

In structural health monitoring (SHM) systems optical fiber sensors are commonly used to collect guided waves. In recent studies fiber Bragg grating (FBG) sensors are used in remote-bonding configuration to capture the guided wave [27,28,43]. In this configuration, the FBG sensor is not directly attached to the structure. Instead, a portion of the optical fiber distant from the FBG sensor is attached to the structure using adhesive bond, through which the fundamental symmetric (S_0) and antisymmetric (A_0) Lamb waves in the structure are converted to propagating fundamental longitudinal (L_{01}) and flexural (F_{11}) waves in the optical fiber. The propagating fundamental waves are then measured with a sensor at a remote location further along the fiber [10,11]. This remote

bonding configuration increases the sensitivity of the FBG to guided waves with small amplitude [10].

Recent studies showed that these propagating acoustic guided waves in optical fibers can be coupled from one fiber to another through a simple adhesively bonded coupler [19,20,30,44]. Leal et al. [19] demonstrated a fiber-optic acoustic splitter by using adhesive to attach a segment of optical fiber to the main sensing fiber at two locations. Using adhesive to fabricate acoustic coupler is more beneficial over previously researched method of using fusion-spliced optical coupler in many ways. Rapid coupling of acoustic wave using adhesive bond allows easy extension of new sensors to an already installed sensing system. Also, since the fibers do not have to be fused to the core level, different sizes and geometries of fibers can also be coupled, which means the fiber exposed to the environment does not have to be a standard single-mode fiber. Kim et al. [30] demonstrated acoustic wave transfer from various kinds of fiber waveguide to a single-mode optical fiber using cyanoacrylate adhesive bond coupler, and showed that the waveform of the L_{01} mode wave is preserved through the adhesive bond coupler. These included multi-mode optical fibers, polyimide-coated silica capillary tubes, and metal fibers. Kim et al. [44] demonstrated an acoustic fiber ring resonator using adhesive bond coupler and showed that the acoustic waves transferring through the adhesive coupler interfere coherently.

There are few researches that investigated the theoretical studies of acoustic wave coupling. Safaai-Jazi [20] theoretically studied the exchange of acoustic power between two cylindrical waveguides with common cladding using the coupled mode theory for lightwave coupling in fused couplers. He predicted that when the diameters of the two waveguides are different, a fraction of the total power oscillates between the two waveguides. He also predicted that when the diameters are identical, complete transfer of power from one waveguide to another is possible. However, the

accuracy of the coupled mode theory for acoustic coupling was not experimentally verified in his work.

Haag et al. [45] introduced an analytical energy model called damper model which mathematically explains the acoustic energy transfer from one waveguide to another in contact. His energy-based model consists of two straight rods having a friction contact line between them, and the energy coupling mechanism is modeled by a viscous damper which connects the differential elements of both waveguides. He compares the energy-based model with experimental and simulation results, providing basis for future studies of multi-wire configurations. Schaal et al. [46] and Zhang et al. [47] demonstrated an improved version of the energy model called spring model, in which the energy coupling mechanism is modeled by a spring instead. The drawback of the damper model is that it is constructed with first order differential equation and thus cannot represent oscillation of energy between the waveguides. Also, if the initial energy of one wire is zero it remains zero, meaning it cannot model a passive wire before energy transfers to it. On the other hand, the spring model is of second order differential equation and thus can represent oscillation of energy between waveguides. Also, the initial energy on a waveguide can be zero in combination with an initial slope to allow for energy transfer. The damper and spring models do not exactly model the acoustic coupler of our interest because in the energy models the waveguides are held together in contact over a long distance, whereas the coupler of our interest is two waveguides that are held together using adhesive material over a short distance. However, the physics of the energy model is identical to our acoustic coupler of interest.

This work explores on the acoustic wave coupling from one fiber waveguide to another via adhesive coupler using finite element analysis (FEA) simulations and compare the results with an analytical model to find out if the analytical model can properly describe acoustic wave coupling

via adhesive coupler. First a detailed FEA model is constructed using COMSOL Multiphysics® software which is very efficient in solving acoustic wave equations and performing parameter sweeps. Using the FEA model, parameter sweep for various input fiber diameters is performed to compare with the past experimental results by Kim et al. [30] for validation of the model. Then three more parameter sweeps are performed for analysis purposes: output fiber diameter, coupler thickness, and coupler length. Lastly, the energy models are compared with the FEA model to see how well they can describe acoustic coupling via adhesive coupler.

4.2 Building FEA Model

For the FEA, COMSOL was used to simulate the acoustic coupling from one optical fiber to another through the adhesive coupler. The design of the model is shown in Figure 4.1. Figure 4.2 shows the overall screenshot of the COMSOL model, and Figure 4.3 shows the screenshot of the coupler region. The initial distance between the surfaces of the two parallel fibers is 1mm, and they come to a contact over 5mm to the adhesive coupler. The length of the coupler is 3.175mm. After the coupler, the two fibers separate back to 1mm over the length of 5mm. On the edge of one end of the input fiber, a displacement of 5.5 cycle Hanning windowed function was excited along the fiber direction as input acoustic wave to simulate L_{01} mode wave. Non-reflective boundaries were applied to the edges of all four branches of the coupler so that there are no back reflections. The optical fibers have silica core, silica cladding, and polyimide coating. For a default single-mode fiber, the coating thickness is 12.5μm and the diameter of silica is 125μm. The coupler is made of cyanoacrylate (CA) adhesive, and the default thickness of the coupler is 12.5μm. To reduce computation time, the geometry of the COMSOL model is divided to two equal pieces along the x-y-plane, and "Symmetry" boundary condition is applied to the cut surface after deleting one of the pieces. Boundaries between different materials are joined together using "Union"

function in which the different materials share the nodes along the boundaries. For the mesh type, triangular meshes are used with predefined “Extra Fine” option with minimum element size of 3.48×10^{-5}m. Measurements were taken every 0.1μs time step at the center of the fibers before the coupler on the input fiber and after the coupler on the output fiber.

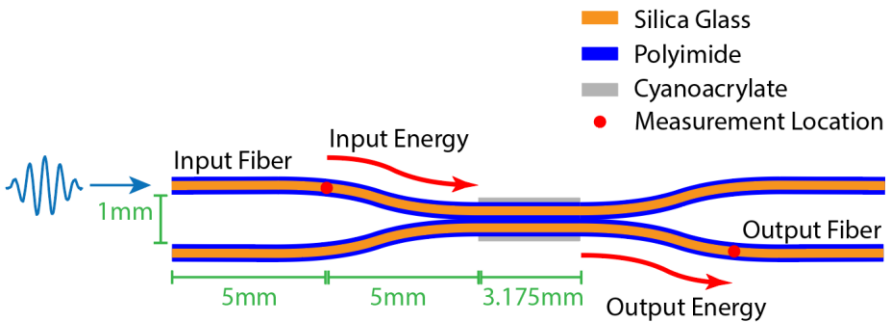

Figure 4.1 Design of the adhesive acoustic coupler.

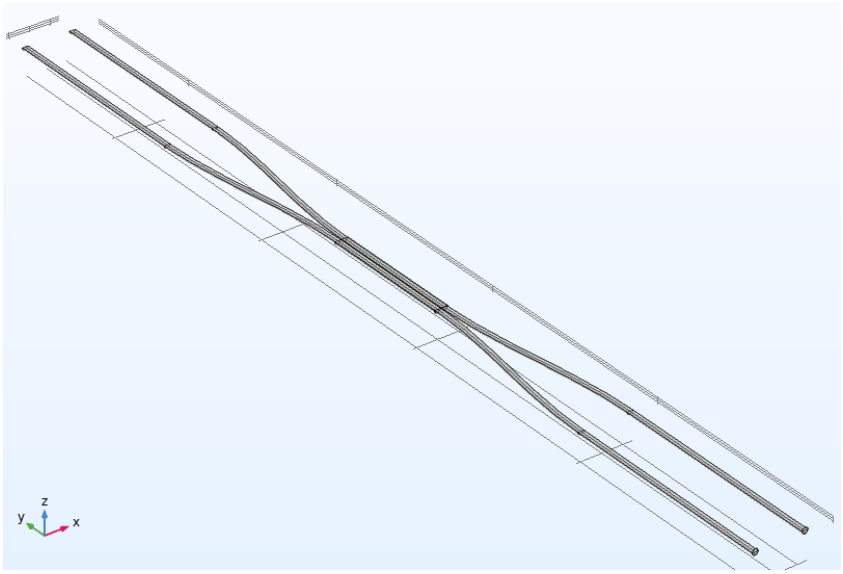

Figure 4.2 Overall COMSOL model of the adhesive acoustic coupler.

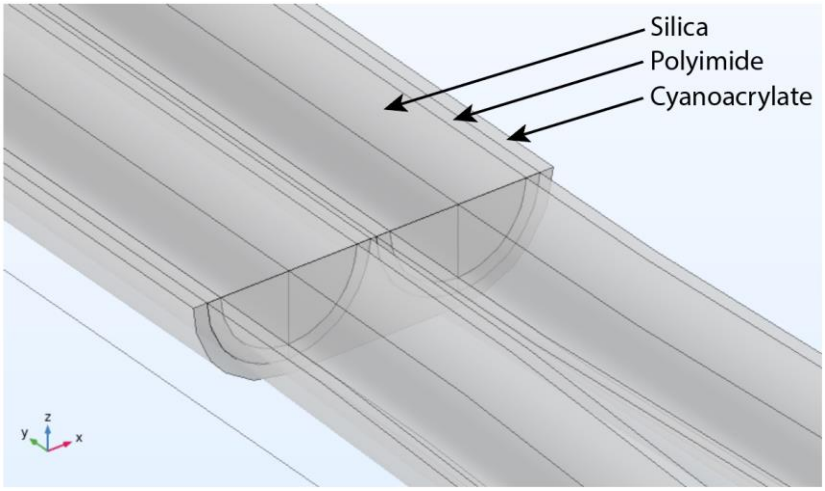

Figure 4.3 Coupler region on the COMSOL model.

4.3 Validation of the Model with Experimental Results using Parameter Sweep

Four parameters are varied in COMSOL to perform parametric sweep: input fiber silica diameter, output fiber silica diameter, the thickness of the coupler adhesive, and the length of the coupler. Following diameters are used for sweeping the input fiber silica diameter: 125µm, and 200µm to 650µm in increments of 50µm. Following diameters are used for sweeping the output fiber silica diameter: 125µm, and 150µm to 650µm in increments of 50µm. Following thicknesses of the coupler adhesive are used: 12.5µm, and 50µm to 275µm in increments of 25µm. Lastly, following coupler lengths are used: 2mm to 4mm in increments of 0.2mm. Figure 4.4 shows the screenshots of the COMSOL model for the parameter sweeps. Figure 4.4(a) shows 600µm-diameter input fiber coupled to a single-mode output fiber, Figure 4.4(b) when the coupler thickness is 275µm, and Figure 4.4(c) when the coupler length is 4mm. Measurements are taken in displacements to directly compare with past experimental results, which was collected using a fiber Bragg grating (FBG) sensor in strain values. The displacement amplitude measurements are squared and the measurement on the output fiber is divided by the measurement on the input fiber

to find the amplitude ratio. Then the results are normalized to the default control case, in which the diameter of silica on both the input and output fibers are 125µm, the coating thickness of the polyimide is 12.5µm, and the coupler thickness is 12.5µm.

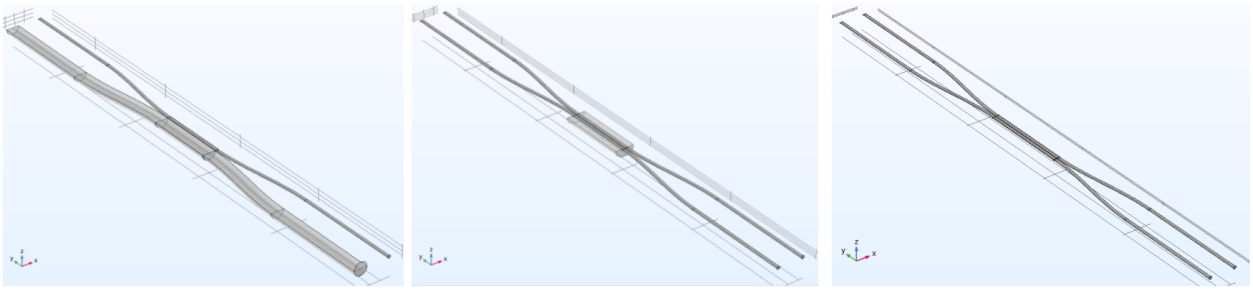

Figure 4.4 Screenshots of the COMSOL model. (a) 600µm-diameter input fiber coupled to a single-mode output fiber, (b) coupler thickness is 275µm, and (c) coupler length is 25.4mm.

Figure 4.5 shows the parametric sweep result for input fiber silica diameter. The result is organized in cross-sectional area of silica instead of the diameter for direct comparison with the past experimental result [30]. It shows that the energy of the coupled L_{01} mode increases with the cross-sectional area of silica, until it reaches a maximum at 0.2mm^2 cross-sectional area. Then the coupled energy decreases with the diameter of silica. This result matches with the experimental results by Kim et al. [30]. They showed that the normalized ratio reaches maximum at 0.15mm^2 cross-sectional area and then decreases because they did not have a fiber with 0.2mm^2 cross-sectional area to experiment with. This shows that the COMSOL model accurately models the actual acoustic coupler behavior and that it is a valid model.

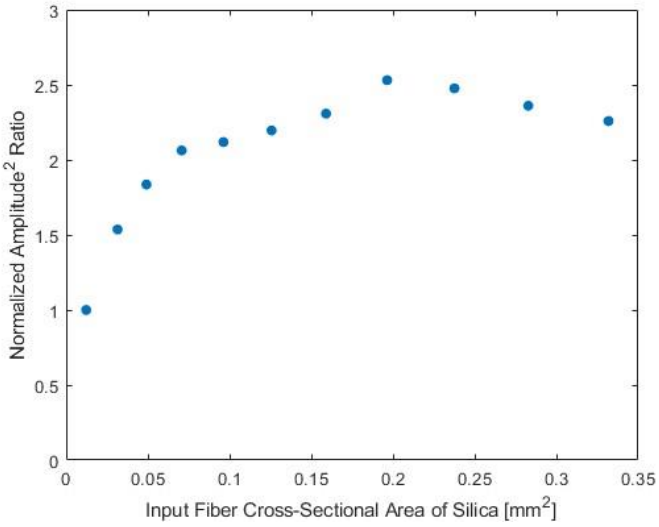

Figure 4.5 Parameter sweep of input fiber silica diameter.

Figure 4.6 shows the parametric sweep result for output fiber silica diameter. The energy ratios are normalized to the same default control case. It shows that the energy of the coupled L_{01} mode decreases exponentially to zero as the diameter of silica increases. This result is reasonable because considering a similar level of energy transfer, the displacement on the larger diameters fiber will be much less than that on the smaller diameter fibers.

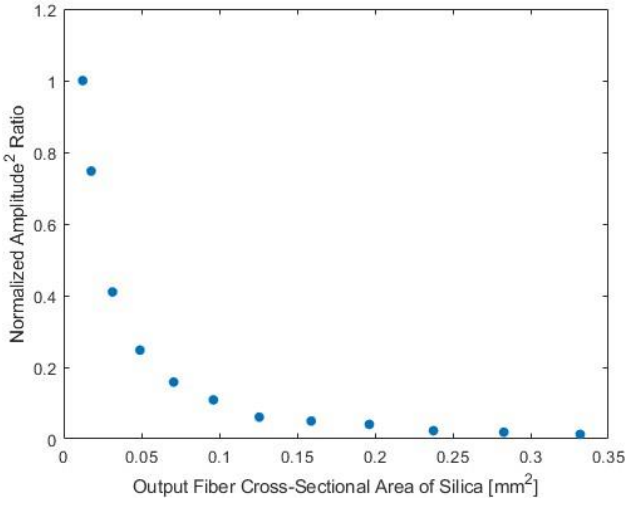

Figure 4.6 Parametric sweep of output fiber silica diameter.

Figure 4.7 shows the parameter sweep result for coupler adhesive thickness. It shows that the energy of the coupled L_{01} mode increases with the coupler thickness until it reaches a maximum at 100µm thickness. After the maximum, the coupled energy decreases approximately linearly with the coupler thickness. Figure 4.8(a)-(c) show the screenshots of the COMSOL model and the input and output fiber displacements when the coupler thickness is 12.5µm, 100µm, and 275µm respectively. Figure 4.8(a) and (b) show that the waveform on the output fiber resembles the waveform on the input fiber, and that the waveforms are preserved. However, Figure 4.8(c) shows that the waveform on the output fiber is not preserved and that the waveform continues after the original 5.5 cycles. This shows that the input wave is dissipated into the coupler and that it is oscillating inside, therefore the energy is spread and the amplitude is low.

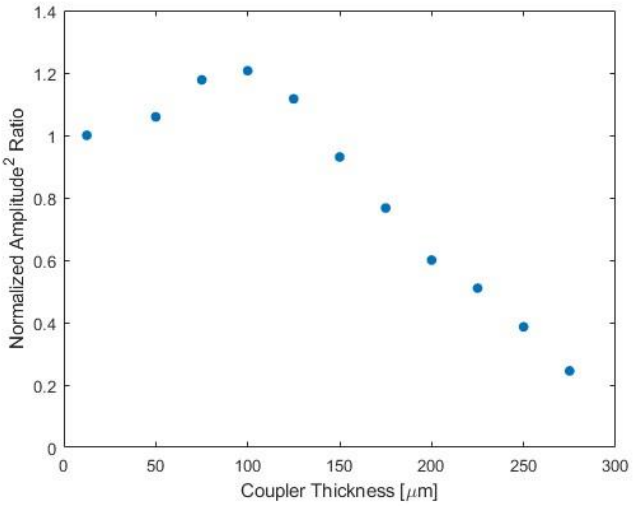

Figure 4.7 Parametric sweep of coupler adhesive thickness.

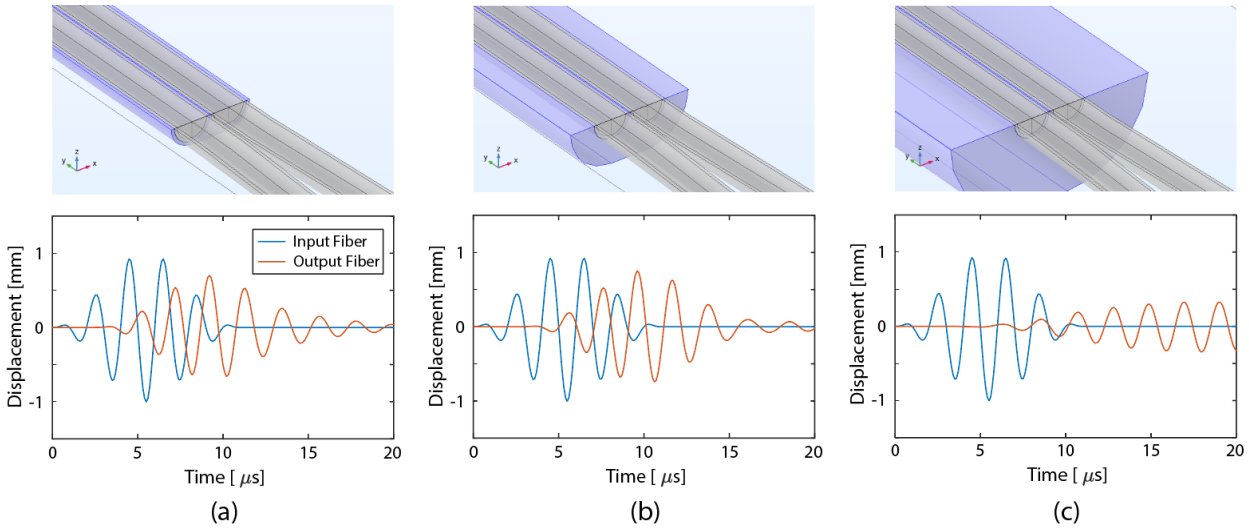

Figure 4.8 Screenshots and the input and output fiber displacements when the coupler thickness is (a) 12.5µm, (b) 100µm, and (c) 275µm.

Figure 4.9 shows the parameter sweep result for coupler length. It shows that the acoustic energy coupled to the output fiber oscillates as the coupler length changes. The oscillation of transferred energy is further analyzed in the later chapters of the paper.

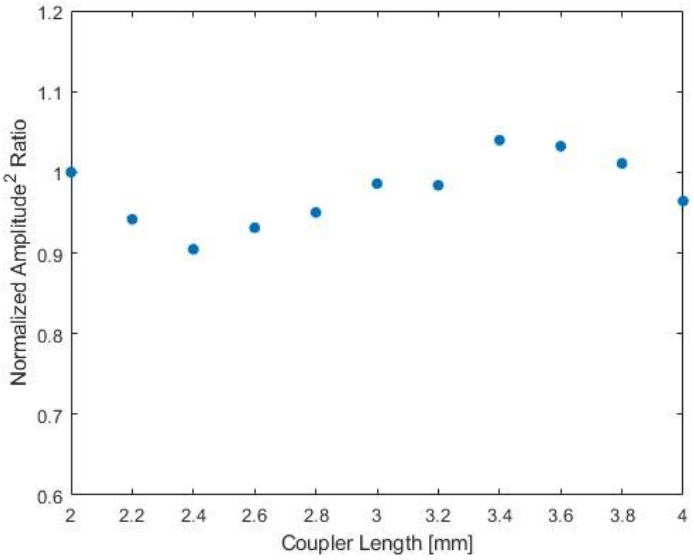

Figure 4.9 Parametric sweep of coupler length.

4.4 Fitting Analytical Model to COMSOL Simulation

The energy models by Haag et al. [45] and Schaal et al. [46] calculates the transfer of propagating acoustic wave from one waveguide to another in contact over long distance. A differential section of a coupled waveguides in contact is shown in Figure 4.10.

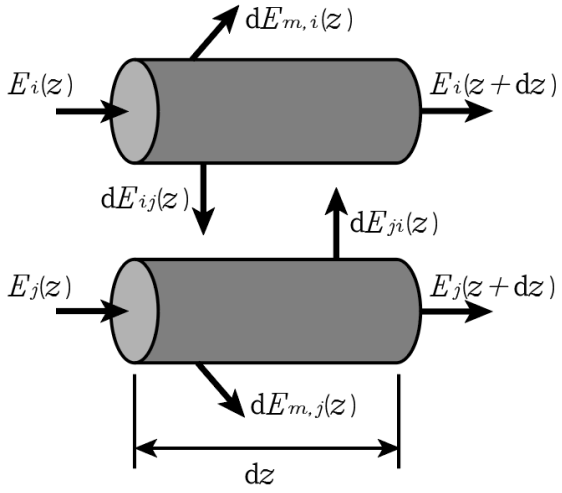

Figure 4.10 Spring modeling of energy transfer between two waveguides.

The displacement field u of a harmonic guided wave in cylindrical waveguides is

$$u(x,t) = \hat{u}(r,\varphi)e^{j(kz-\omega t)} \tag{4.1}$$

where r is the radius of the waveguide, φ is the angle, k is the wavenumber, z is the distance along the waveguide, ω is the angular frequency, and t is time. The total energy E can then be expressed as

$$E(t) = \int_0^R \int_0^{2\pi} \frac{1}{a_R^2} \rho \hat{u}(r,\varphi) \cdot \hat{u}(r,\varphi) r d\varphi dr \cdot \int_{z_0}^{z_1} \frac{d}{dt}\left(a_R e^{j(kz-\omega t)}\right)^2 dz \tag{4.2}$$

where ρ is the mass density and $a_R = \hat{u}_r(r = R)$ is the radial amplitude of the wave on the surface of the waveguide. By taking out the integrals over φ and r, Equation (4.2) becomes

$$E(t) = const \cdot \int_{z_0}^{z_1} \dot{u}_R^2(z,t)dz \tag{4.3}$$

By using the energy transport velocity c_g and the relation $dz = c_g dt$, Equation (4.3) becomes

$$E(t) = const \cdot \int_{t_S}^{t_F} \dot{u}_R^2(z,t)c_g dt = const \cdot \int_{t_S}^{t_F} \dot{u}_R^2(z,t)dt \tag{4.4}$$

where the wave packet is now analyzed in the time interval $[t_S(z), t_F(z)]$ for a position z, instead of in the spatial domain for an instant in time.

The equation of energy of traveling wave for a section of waveguide i is

$$E_i(z) = E_i(z + dz) + dE_{m,i}(z) + dE_{ij}(z) \tag{4.5}$$

where $dE_{m,i}$ is the dissipated energy from the waveguides due to material damping and dE_{ij} is the energy transferred from waveguide i to j. The dissipated energy is

$$dE_{m,i}(z) = C_m E_i(z)dz \tag{4.6}$$

where C_m is the material damping coefficient.

The difference between damper model and spring model is that the damper model uses viscous damper as the energy coupling mechanism between the two waveguides, and the spring model uses spring as the energy coupling mechanism between the waveguides. For the spring model, the coupling term E_{ij} can be derived from the force F_{ij} of the spring

$$F_{ij} = k\big(u_{R,i} - u_{R,j}\big) \tag{4.7}$$

where k is the spring constant. The kinetic energy transferred from the waveguide i to j is then

$$dE_{ij}(z) = F_{ij}\dot{u}_{R,i}dt = k\big(u_{R,i} - u_{R,j}\big)\dot{u}_{R,i}dt \tag{4.8}$$

The square root of the kinetic energy is $E_i = \frac{1}{\alpha^2}\dot{u}_{R,i}^2$ where α is a real number normalization constant, therefore $\dot{u}_{R,i} = \alpha\sqrt{E}$. Then Equation (4.8) can be written as

$$d^2E_{ij}(z) = \left[k\left(\alpha\sqrt{E_i} - \alpha^2\sqrt{E}_j\right)\alpha\sqrt{E_i} + k\left(u_{R,i} - u_{R,j}\right)\ddot{u}_{R,i}\right]dt^2 \tag{4.9}$$

Since $\ddot{u}_{R,i} = 0$, Equation (4.9) becomes

$$d^2E_{ij}(z) = k\left(\alpha\sqrt{E_i} - \alpha^2\sqrt{E}_j\right)\alpha\sqrt{E_i}\,dt^2 \tag{4.10}$$

Then by using the group velocity $c_g = \frac{dz}{dt}$ and coupling coefficient $K_c = \frac{k\alpha^2}{c_g^2}$, Equation (4.10) becomes

$$d^2E_{ij}(z) = K_c\left(\sqrt{E_i} - \sqrt{E}_j\right)\sqrt{E_i}\,dz^2 \tag{11}$$

By using the Equations (4.5), (4.6), and (4.11), and taking the initial conditions $E_i(0) = E_{i,0}$ and $\frac{dE_i(0)}{dz} = E'_{i,0}$ the non-linear differential equation for the waveguide i in contact with waveguide j and vice versa are given by

$$\begin{aligned}
\frac{d^2E_{ij}(z)}{dz^2} &= -C_m\frac{dE_i(z)}{dz} - K_c\left(\sqrt{E_i(z)} - \sqrt{E_j(z)}\right)\sqrt{E_i(z)} \\
\frac{d^2E_{ji}(z)}{dz^2} &= -C_m\frac{dE_j(z)}{dz} - K_c\left(\sqrt{E_j(z)} - \sqrt{E_i(z)}\right)\sqrt{E_j(z)}
\end{aligned} \tag{4.12}$$

For the damper model, the coupling term E_{ij} can be derived from the force F_{ij} of the damper

$$F_{ij} = c\left(\dot{u}_{R,i} - \dot{u}_{R,j}\right) \tag{4.13}$$

where c is the damper constant. Using the similar method and the coupling coefficient $C_c = \frac{c\alpha^2}{c_g^2}$ we can derive the first order ordinary nonlinear differential equations for the damper model:

$$\begin{aligned}
\frac{dE_{ij}(z)}{dz} &= -C_mE_i(z) - C_c\left(\sqrt{E_i(z)} - \sqrt{E_j(z)}\right)\sqrt{E_i(z)} \\
\frac{dE_{ji}(z)}{dz} &= -C_mE_i(z) - C_c\left(\sqrt{E_j(z)} - \sqrt{E_i(z)}\right)\sqrt{E_j(z)}
\end{aligned} \tag{4.14}$$

Since the damper model is constructed with 1st order ODE, it cannot represent oscillation of energy between the waveguides. Also, if the initial energy of one waveguide is zero then it remains zero, thus it cannot model a passive wire before energy transfers to it. The spring model on the other hand is constructed with 2nd order ODE, so it can represent oscillation of energy between waveguides. Also, the initial energy on a waveguide can be zero in combination with an initial slope of energy to allow for energy transfer.

To compare the simulation results to the energy models, few changes are made to the COMSOL model. First, the length of the coupler is changed from 3.175mm to 15mm. Also, the results are recorded in velocity squared values instead of displacement squared values because energy is a constant times the velocity squared, and velocity squared ratio is equal to energy ratio.

Figure 4.11 shows the velocity squared plot of the two fibers along the contact region i.e., the coupler. The values are normalized to the initial input velocity squared values. The data for $z = [0, 0.3]\text{mm}$ is not plotted because there is numerically a sudden change of velocity at the beginning of the coupler boundary. It shows that there is a clear oscillation of energy between the input and the output fiber for approximately $z = [0.3, 8]\text{mm}$, which is the same behavior described by the spring model [46] and the coupled mode theory [20]. However, from around 10mm the energy level in the two fibers start to level out and then oscillate together, which is not the kind of behavior described in the coupled mode theory. This is because in optics the damping is extremely minimal and thus is not considered in the coupled mode theory. Since the energy levels of the input and output waveguide are oscillating, we can rule out the damper model and only fit the spring model.

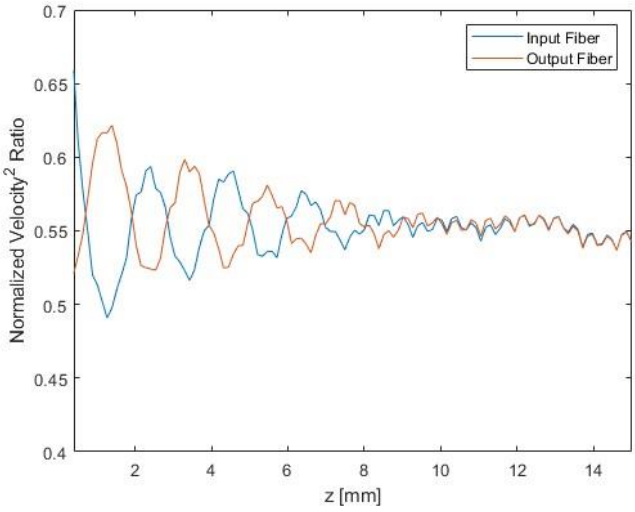

Figure 4.11 Velocity squared ratio of input and output fiber along the coupler.

To analyze how well the spring model can be fitted to the COMSOL model, first the diameter of the output fiber on COMSOL is varied and the spring model was fitted to the simulation results to analyze how the energy model coefficients are affected. To fit the spring model to the simulation results, the two coefficients, K_c and C_m, and four initial conditions, $E_{i,0}, E_{j,0}, \frac{dE_{i,0}}{dz}$, and $\frac{dE_{j,0}}{dz}$, are manually fitted to calculate the energy ratios.

Figure 4.12 shows the normalized energy in the input and output fibers produced using the COMSOL simulation. The input fiber is the default fiber, and Figures 4.12 (a)-(d) show the results when the diameter of the output fiber D_{output} is 125μm, 150μm, 180μm, and 210μm respectively. They show that as the output fiber diameter increases, the equilibrium energy, to which the normalized energy of input and output fibers approach, decreases. Also, the period of the oscillation of energy increases as the fiber diameter increases.

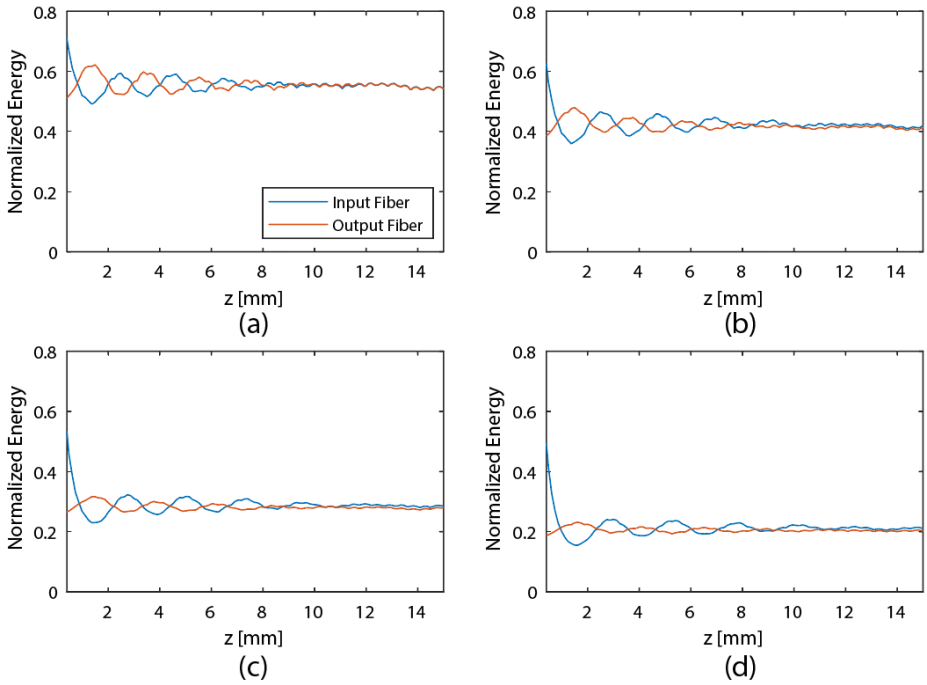

Figure 4.12 COMSOL simulation of output fiber diameter change. (a) $D_{output} = 125\mu m$, (b) $D_{output} = 150\mu m$, (c) $D_{output} = 180\mu m$, and (d) $D_{output} = 210\mu m$.

Figure 4.13 shows the spring model fitted to the COMSOL simulations. The K_c and C_m values for each output diameter case are shown in Table 4.1. The coupling coefficient K_c majorly determines the period of the oscillation of two energy levels, and the material damping coefficient C_m majorly determines the value of the equilibrium energy and how fast the oscillation of energy damps out. Table 4.1 shows that the diameter of the output fiber does not affect C_m, but as the diameter of the output fiber increases, K_c decreases linearly. This shows that even though the dimensions of the waveguides are not input variables in the spring model, it is still captured in the model through the boundary conditions and the K_c values

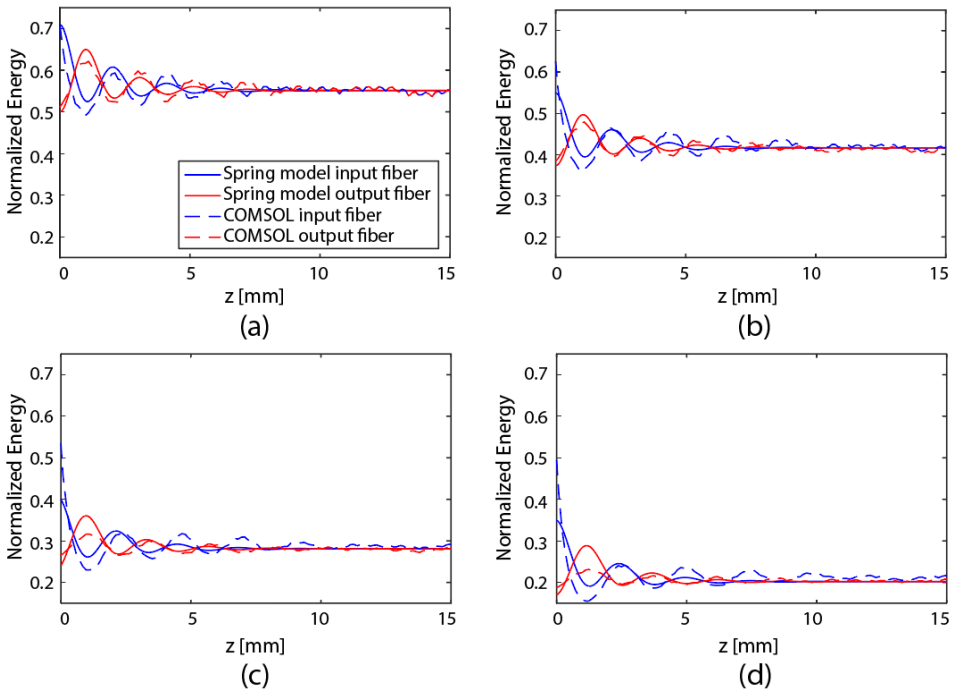

Figure 4.13 Spring Model fitted to the simulation. (a) $D_{output} = 125\mu m$, (b) $D_{output} = 150\mu m$, (c) $D_{output} = 180\mu m$, and (d) $D_{output} = 210\mu m$.

Table 4.1 K_c and C_m values for output fiber diameter variation.

R_{output} $[\mu m]$	**62.5**	**75**	**90**	**105**
K_c	9.5×10^6	8.5×10^6	7.5×10^6	6.5×10^6
C_m	1000	1000	1000	1000

One thing to note is that the radius of the waveguide is only incorporated in the energy model as the velocity at the surface of the waveguide $\dot{u}_R$ in Equation (4.3). The experimental results from Kim et al. [30] and the COMSOL results from Figure 4.5 show that the energy transfer from the input fiber to the output fiber drops significantly when there is a huge fiber diameter mismatch, and this behavior is not incorporated in the energy model which treats the system as a

perfect system. Thus, the spring model cannot properly model the decrease in the coupling efficiency due to poor contact between the fibers when the fiber size mismatch is great.

Next the spring model is fitted to a system where the CA adhesive coupler induces attenuation. In experimental environment, the CA polymer material used for the coupler to hold the two fibers together will always induce loss of energy due to damping. To simulate this, Rayleigh damping coefficient β_{dK} is applied to the CA polymer material in the COMSOL model. Plots are generated using multiple values of Rayleigh damping coefficient, and the results are shown in Figure 4.14. It shows that as β_{dK} increases, the equilibrium energy of input and output fibers decreases to zero at faster rate and the period of oscillation increases. The spring model cannot be fitted to the energy behavior caused by Rayleigh damping on the coupler material shown in Figure 4.14. This is due to the physical limitation of the energy model. The energy model is designed to calculate the acoustic energy transfer between waveguides in contact, whereas in our adhesive coupler of interest there is a polymer material holding the two fibers in contact.

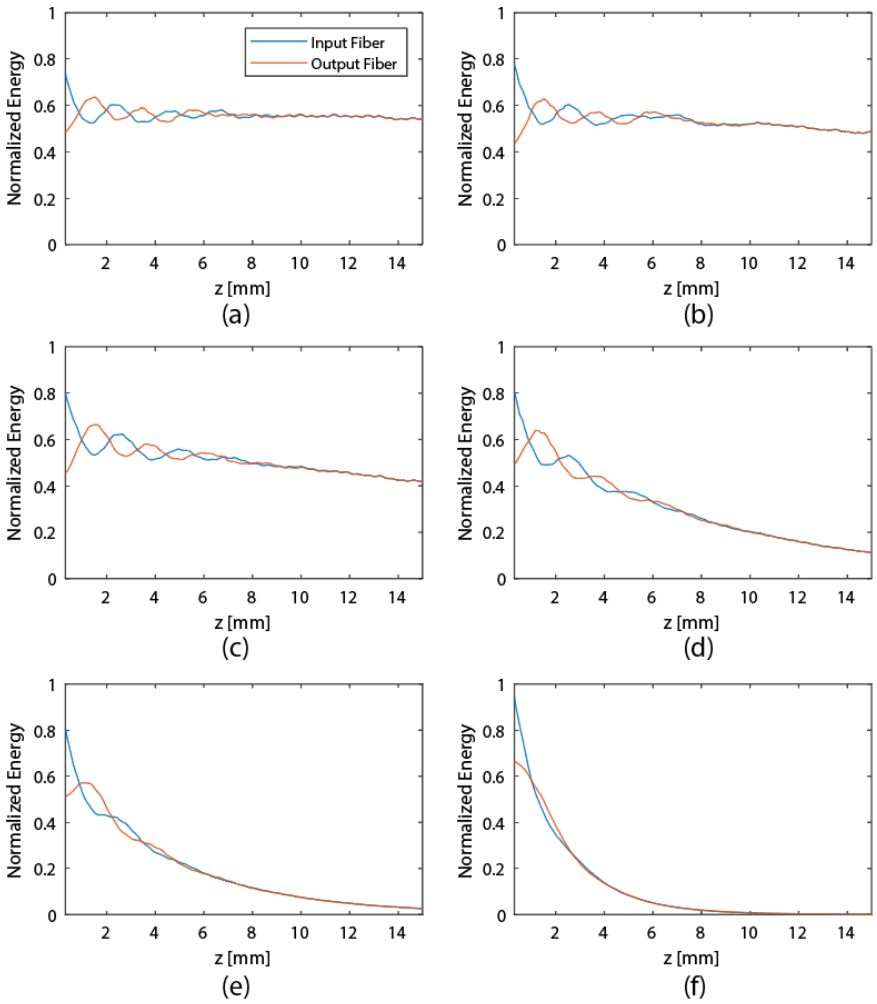

Figure 4.14 Effect of Rayleigh coefficient on the energy transfer behavior. (a) $\beta_{dK} = 0.1\mu s$, (b) $\beta_{dK} = 0.5\mu s$, (c) $\beta_{dK} = 1\mu s$, (d) $\beta_{dK} = 5\mu s$, (e) $\beta_{dK} = 10\mu s$, and (f) $\beta_{dK} = 50\mu s$.

4.5 Conclusions

The results from this paper demonstrate that the ODE spring model has the potential to properly describe the behavior of acoustic coupling from one optical fiber to another via an adhesive coupler. It properly describes the oscillating transfer of energy between the two fibers. Further refinements to the model could be made to expand the utility of the model. The model is governed by two coupler parameters and four initial conditions. For this work the coupler

parameters were empirically fit to the finite element results, however, the ability to predict the coupler parameters from a known coupler geometry would increase the benefit of the ODE model. Similarly, a more rigorous method to choose the initial conditions would make the model more useful. The spring model is limited to the ideal case scenario, and therefore it cannot properly model the decrease in energy transfer when the fiber size mismatch is very large. This difference is most likely due to the non-ideal geometry in the fabricated coupler once the size mismatch was too large. As the power transferred starts to decrease at this point in the experiments, this is not likely a coupler geometry of interest for actual applications. Finally, the ODE model does not include the coupler material behavior in its calculations and therefore cannot model the damping caused by it. However, we can easily incorporate an effective attenuation per unit length in future work to incorporate the attenuation caused by the coupler material.

4.6 Acknowledgement

The authors thank the Office of naval Research (ONR) (N00014-19-1-2053) for the financial support of this research.

Chapter 5

Extension of Fiber Bragg Grating Sensor Network by Acoustic Wave Coupling using Simple Adhesive Coupler

Previous studies demonstrated coupling of acoustic guided wave from one optical fiber to another through a simple adhesive bond coupler. This paper experimentally utilizes such adhesive bond coupler to easily extend an already existing sensor network. We experimentally demonstrate this concept for detecting simulated cracks growing from circular holes in a thin aluminum plate. A single, remotely bonded FBG sensor is used to detect the original crack growth, followed by the addition of other optical fiber segments using adhesive couplers to detect at new crack growth locations on the plate. A laser Doppler vibrometer is also used to measure the guided wave propagation through the plate to verify that the changes in the FBG sensor measurements are due to the growth of the cracks.

5.1 Introduction

Fiber Bragg grating (FBG) sensors are commonly applied to detect ultrasonic guided waves for structural health monitoring (SHM) applications [21]. Recently FBG sensors have been applied in the remote bonding configuration, which can increase the sensitivity of the sensor to the low amplitude guided waves [10,27,28,43]. In this configuration, the ultrasonic wave in the structure is coupled into the optical fiber and converted into a longitudinal wave propagating along the fiber [22]. Multiplexing of these ultrasonic waves from multiple optical fibers into a single optical fiber can also be achieved through a simple, adhesively bonded acoustic coupler [19,30,44]. Since it is not necessary to transfer optical modes between the fibers, fusion splicing of the fibers is not required. Kim et al. [30,44] showed that the waveform of the input longitudinal mode is preserved after passing through the adhesive bond coupler.

An additional benefit to adhesive coupling not previously explored is that new sensors can easily be added to an installed optical fiber sensor network. Splicing or recoupling a new sensing fiber is not practical for some field applications where the optical fibers are mounted to a structure [48]. By utilizing simple adhesive bond couplers, optical fibers could be attached at new locations to the original sensing fiber.

In this letter we experimentally demonstrate this concept for detecting simulated cracks growing from circular holes in a thin aluminum plate. A single, remotely bonded FBG sensor is used to detect the original crack growth, followed by the addition of other optical fiber segments to detect at new crack growth locations on the plate. The additional sensors are connected to the original remotely bonded FBG through an adhesive coupler. A high-resolution 3-dimensional laser Doppler vibrometer (LDV) (3D MSA, Polytec) is also used to measure the guided wave propagation through the plate to verify that the changes in the FBG sensor measurements are due to the growth of the cracks.

5.2 Experimental Setup

Figure 5.1 shows an overview of the experimental setup. The 6061 aluminum plate dimensions are 30.48 cm x 30.48 cm with 0.8 mm thickness. A water jet was used to cut out three holes with 2.54 cm diameter, each 5.08 cm apart in the plate. Then electrical discharge machining (EDM) was used to produce 2 mm long pre-cracks on both sides of each hole. A picture of the hole region in the plate is shown in Figure 5.2.

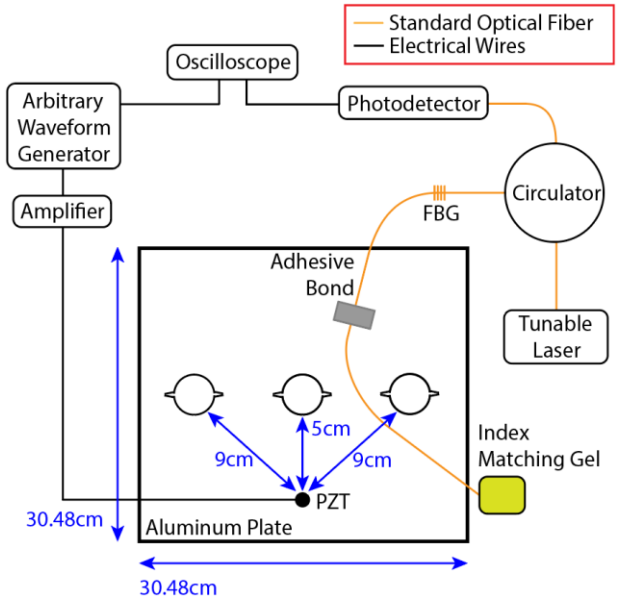

Figure 5.1 Experimental setup for the damage detection.

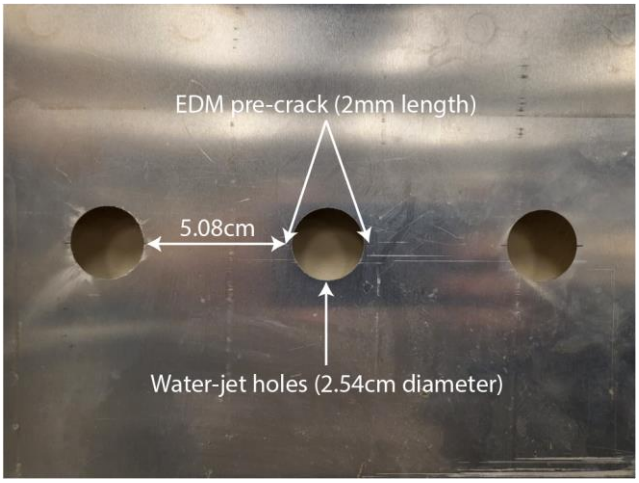

Figure 5.2 Picture of the aluminum plate sample.

The input Lamb wave was generated in the aluminum plate by exciting a Hanning windowed function of 5.5 cycles at 300 kHz using a piezoelectric transducer (PZT). The PZT is driven by an arbitrary waveform generator (AWG) and amplifier. The PZT was bonded to the surface of the plate 5cm away from the center hole and 9cm away from the adjacent holes using

cyanoacrylate (CA) adhesive. The plate boundaries were covered with an elastomeric damping material (Dynamat®) to eliminate boundary reflections.

A standard 125 μm single-mode polyimide coated silica optical fiber is attached to the plate sample using a thin layer of 2 cm x 1 cm cyanoacrylate (CA) adhesive. For consistency and repeatability of the adhesive, a rectangular area of 2 cm x 1 cm was marked with Kapton® tape over the fiber on the plate, and a scraper was used to spread the adhesive over the area. The Kapton® tape was removed after curing the adhesive for 3 hours.

The Lamb waves from the plate are converted into a longitudinal (L_{01}) mode wave in the optical fiber through the adhesive [22]. A FBG sensor with 1560 nm Bragg wavelength and 10 mm length is embedded in the main sensing fiber to measure the L_{01} mode wave. One end of the sensing fiber was connected to the tunable laser and photodetector through an optical circulator. The output response from the FBG was measured by tuning the tunable laser output to the rising edge of the FBG spectrum and measuring the change in amplitude of the reflected signal. The loose end of the sensing fiber was submerged in index matching gel to minimize optical and acoustic wave reflections.

Figure 5.3 shows the series of crack and sensing configurations tested in this paper. Initially the sensor, a single crack, and the PZT will be positioned in a straight line (Figure 5.3(a)). Then a second crack is added not between the PZT and the first sensor (Figure 5.3(b)). As the first sensor would not be able to well detect the second crack, a second sensor will be added to the structure in line with the PZT (Figure 5.3(c)). Next, a third crack will be added to the structure at another location not aligned with the first two sensors (Figure 5.3(d)) and a third sensor will be added to detect it (Figure 5.3(e)).

To fabricate the acoustic couplers, the ends of optical fiber segments were cleaved and positioned in contact with the main fiber, and 3.175 mm was marked using Kapton® tape and CA adhesive was applied over the fibers. A schematic of the 2x1 and 3x1 acoustic couplers used are shown in Figure 5.4. When fabricating the 3x1 acoustic coupler, the 2x1 acoustic coupler was removed and 3x1 coupler was fabricated from scratch instead of adding a fiber to the 2x1 acoustic coupler. The adhesive was cured for 3 hours. The length of the three fiber segments between the plate and adhesive coupler were different (see Figure 5.3) so that the signals from each bond location arrived at the FBG time separated

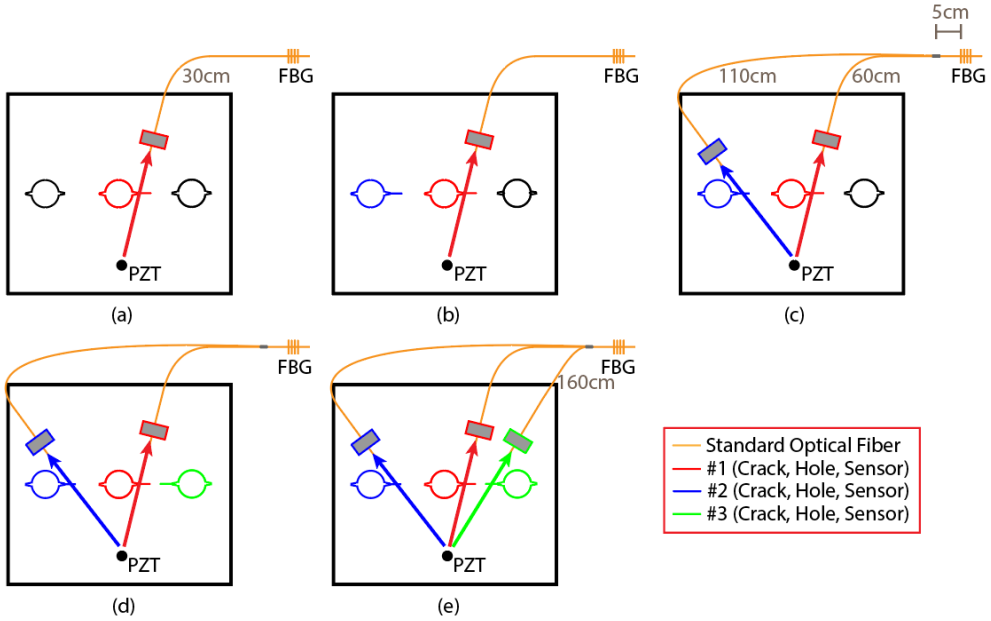

Figure 5.3 Crack and sensing configurations tested in this paper. (a) 1 crack, 1 sensor; (b) 2 cracks, 1 sensor; (c) 2 cracks, 2 sensors; (d) 3 cracks, 2 sensors; (e) 3 cracks, 3 sensors.

Figure 5.4 Sketch of the (a) 2x1 and (b) 3x1 acoustic coupler.

5.3 Single Damage Location

As shown in Figure 5.3(a), the adhesive bond, the crack growth region, and the PZT were placed in a straight line for the first test. A razor blade was used to increase the pre-crack length in increments of 2 mm between each measurement. Figure 5.5 plots the FBG measurements for three different pre-crack lengths, averaged over 4096 data sets. Based on the wave velocities in the plate and fiber, the wave that arrives at 90 μs is the L_{01} mode wave coupled from the S_0 wave from the plate, and the wave that arrives at 120 μs is the L_{01} mode wave coupled from the A_0 wave from the plate. There are additional vibrations present superimposed on the Hanning windowed signal, which are likely the signals reflected from the adjacent holes arriving with a delay. We will only use the L_{01} mode wave coupled from the S_0 wave in the discussion because it has a higher measured amplitude. Figure 5.6 plots the measured peak-to-peak amplitude of the L_{01} mode wavepacket as the crack length increased. Measurements at 12mm and 18mm are skipped by mistake because the crack length was increased manually. It shows that with increasing crack length the amplitude of the L_{01} mode wave decreased, meaning the sensor is sensitive to the propagation of damage at crack #1.

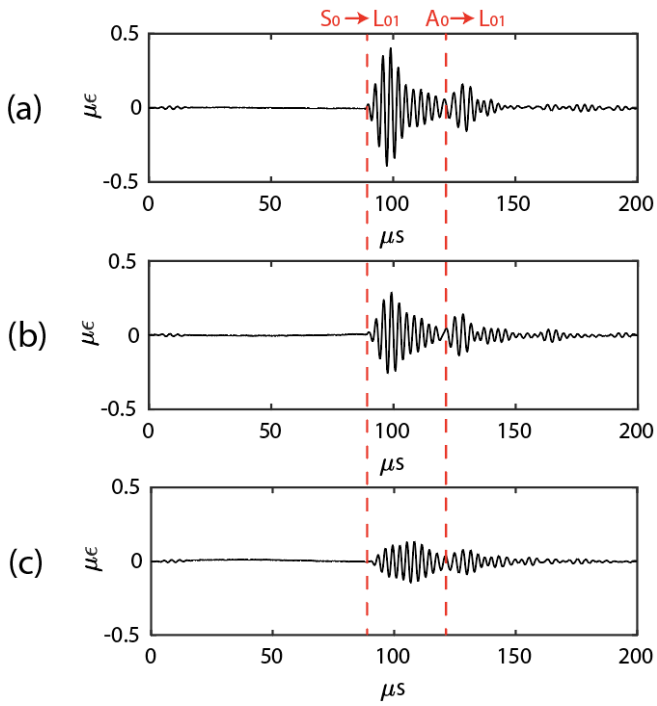

Figure 5.5 FBG measurements for (a) 2 mm pre-crack, (b) 10 mm and (c) 20 mm crack for 1 damage location.

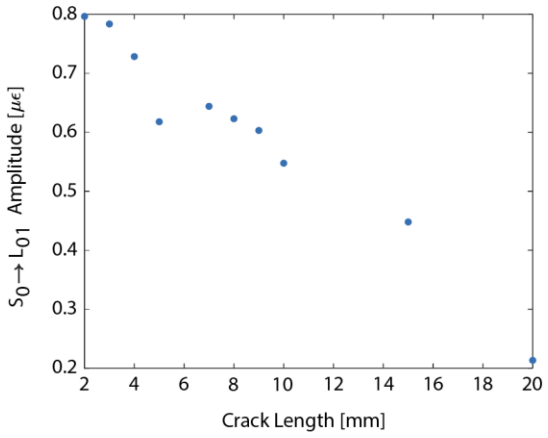

Figure 5.6 Peak-to-peak amplitude on the wave from sensor #1 as crack #1 length increases.

To better understand the change in FBG measurements with crack length, the plate surface velocity was measured with the LDV to map the propagation of the guided waves in the aluminum

plate. Measurements were averaged over 1500 excitations at a sample frequency of 6250 kHz. Figure 5.7(a) shows the picture of the actual sample with the scan region marked with black ink. The scan region is coated with weld check spray to reduce reflections from the aluminum surface. The regions immediately around the PZT, hole, and optical fiber adhesive bond are not flat and are difficult to resolve with the 3D LDV, therefore they were removed from the scan region.

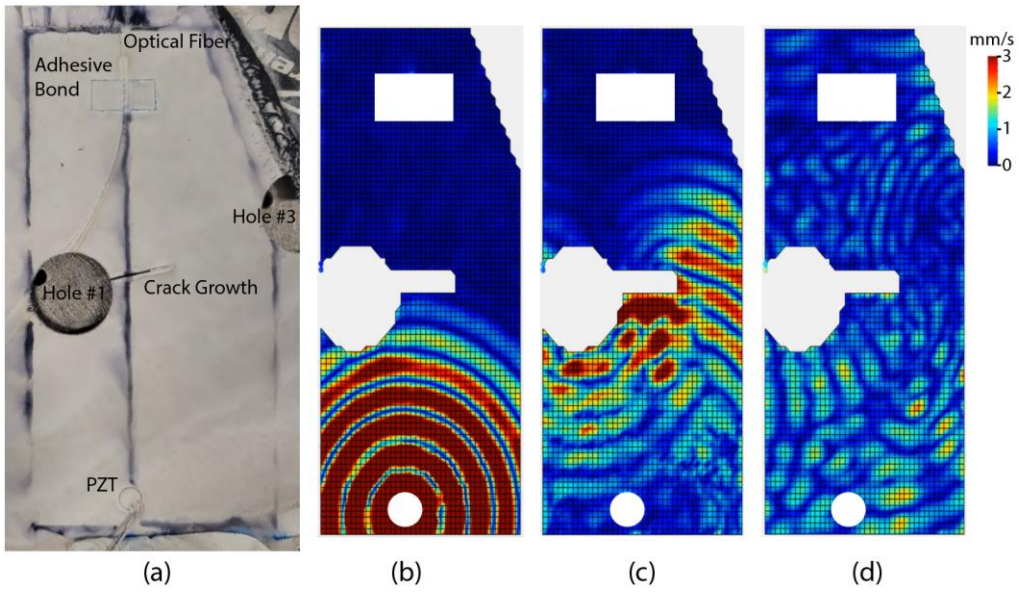

Figure 5.7 (a) Picture of the LDV scan region, (b) surface velocity measurement at 20 µs, (c) 25 µs, and (d) 70 µs.

Figures 5.7(b)-(d) show the LDV velocity measurements for a crack length of 20 mm. Figure 5.7(b) shows the propagation of circular Lamb waves spreading out from the PZT in the structure, at 20 µs after excitation, as expected. Figure 5.7(c), at 25 µs, shows that a fraction of the waves reflect backwards at the hole and pre-crack opening and a fraction of the waves go around the pre-crack. Figure 5.7(d), at 70 µs, shows that the waves propagating around hole #1 to the right are reflected from the adjacent hole #3 and interfere with the waves propagating around hole #1 to

the left at the adhesive bond region. These LDV measurements on Figure 5.7 confirm that the additional vibrations from the FBG measurements on Figure 5.5 are caused by the waves reflecting from and going around the adjacent holes. In addition, they explain the slight delay in arrival time of L_{01} mode coupled from the S_0 mode on Figure 5.5(c) compared to that from Figure 5.5(a) because the signal does not travel through the crack but around it, increasing the propagation distance.

5.4 Multiple Damage Locations

Next, as shown in Figure 5.3(b), a second crack was extended from the hole on the left. An optical fiber was then bonded to the plate at another location (sensor #2) that is in line with a secondary crack region (crack #2), and one end of the fiber was coupled to the main sensing fiber using a 2x1 acoustic coupler (Figure 5.3(c)). FBG measurements were taken while increasing the length of crack #2 every 2 mm.

Figure 5.8 plots the FBG measurements at 2 mm, 10 mm, and 20 mm crack lengths respectively (crack #2). There are two wave packets present in the measurements: the wave from Sensor #1 which arrives at around 150 μs, and the wave from Sensor #2 which arrives at around 240 μs. The wave packets were isolated in time by controlling the length of each optical fiber segment. Note that the wave packet at 150 μs is identical to the wave packet from Figure 5.5(c) because the 2nd sensor was added after the first experiment. As the crack length increases, the L_{01} waveform measured by sensor #2 decreases, as observed for the previous case discussed in Section II. The waveform measured by sensor #1 also changed, but not in a monotonic trend.

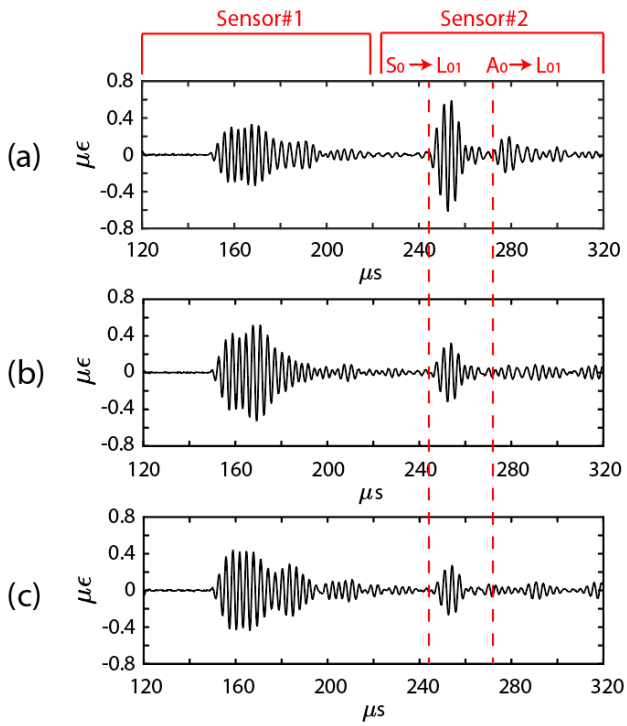

Figure 5.8 (a) FBG measurements taken for 2 mm crack (crack #2), (b) 10 mm, and (c) 20 mm for 2 damage locations.

Figure 5.9 plots the peak-to-peak amplitudes of the L_{01} wavepacket from sensors #1 and #2 as crack #2 length increased. The plot shows that there are minor changes in the wave amplitude measured from sensor #1 as crack #2 length increased, which is because crack #2 affected the reflection of wave from hole #2. However, the changes are not significant and are complicated by the fact that multiple waveforms are overlapped in the signal and the arrival time of the second wavepacket changed with the crack length. Figure 5.9 also shows that the amplitude of wave from sensor #2 decreased as crack #2 length increased. These results show that the system was able to detect crack #2 with sensor #2, but not with sensor #1.

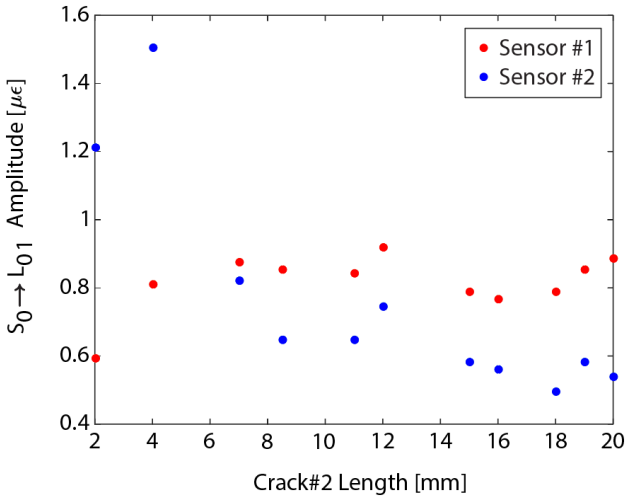

Figure 5.9 Peak-to-peak amplitude of the wave from sensor #1 and sensor #2 as crack #2 length was increased.

Then as shown in Figure 5.3(e), the third crack was propagated and a new optical fiber was bonded to the plate (sensor #3) in line with crack #3 and coupled to the main sensing fiber using the same acoustic coupler. Experiments were repeated while increasing the length of crack #3 by 2 mm. Figure 5.10 plots the peak-to-peak amplitudes of the waves from Sensors #1, #2, and #3 as the length of crack #3 increased. Measurements from sensor #1 show that there is an increase in the amplitude as crack #3 length increased. Measurements from sensor #2 show no significant amplitude change in the wave as crack #3 length increased. Lastly, measurements from sensor #3 show that there is a significant decrease in amplitude of wave as crack #3 length increased. These results demonstrate that Sensor # 2 was not able to detect the increase of crack #3. Sensor #1 was able to detect the crack, because the locations of sensors #1 and #3 were close. However by adding sensor #3 to the system more information about crack #3 could potentially be gathered.

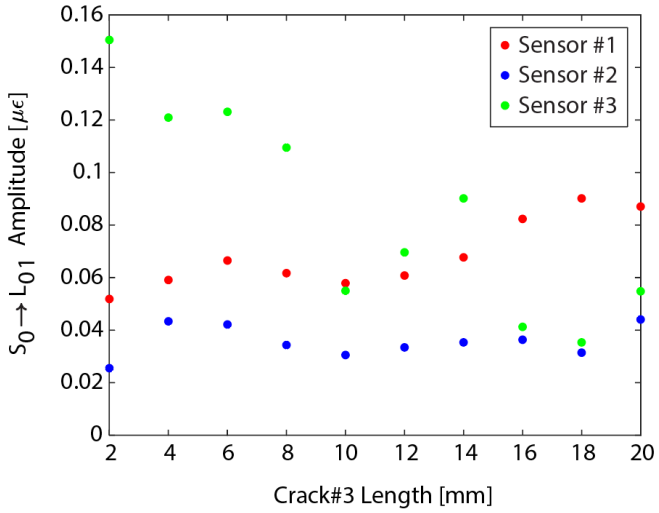

Figure 5.10 Peak-to-peak amplitude on the wave from Sensor #1, Sensor #2, and Sensor #3 as Crack #3 length was increased.

Figure 5.11 shows the LDV measurement of the aluminum plate sample in the region around the PZT and sensors #1 and #3. Figure 5.11(a) shows the picture of the sample with the scan region marked with black ink. Figure 5.11(b) and (c) plot the LDV measurements at 20 µs and 30 µs after the excitation respectively. In Figure 5.11(c) we see that a portion of the waves are reflected from the two holes and cracks, and a portion propagate through the opening of the two cracks. This narrow opening acts like a new wave source, and the wave that propagate through forms circular waves. This change in the propagation of wave compared to having only one crack contributed to the increase in the amplitude of wave captured in sensor #1 with increasing crack length.

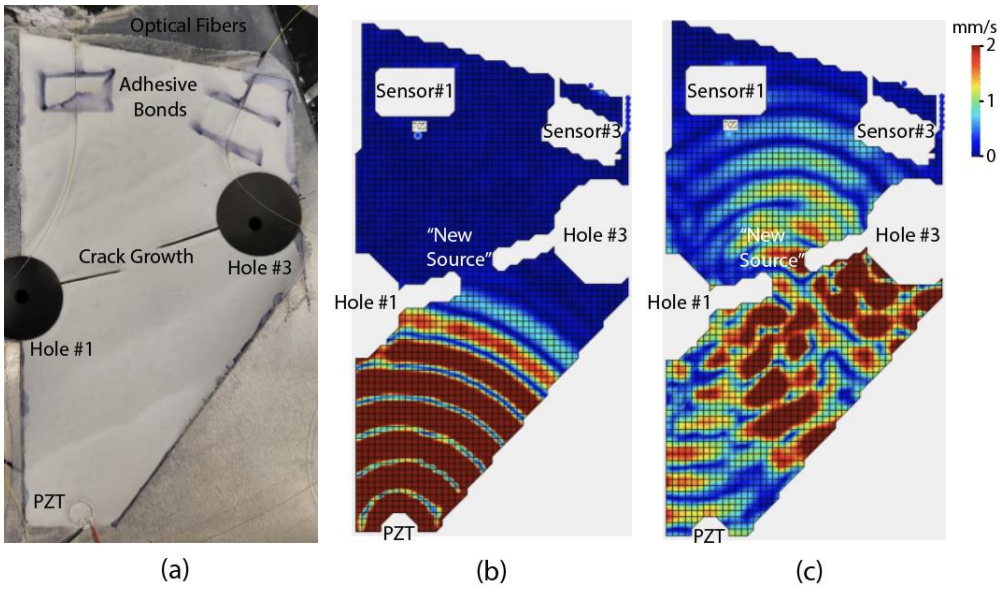

Figure 5.11 (a) Picture of the LDV scan region, (b) LDV measure at 20 μs after excitation, and (c) 30 μs after excitation.

5.5 Conclusions

This study experimentally demonstrates an easy method to extend an already installed FBG sensing system for ultrasonic waves by coupling optical fiber segments to the sensing fiber using an adhesive bond coupler. Experiments were performed as the number of fiber segments coupled to the sensing fiber was increased. A LDV was used to measure the vibration on the structure to demonstrate that the FBG measurements were consistent with the wave propagation in the plate. By coupling the wave from the structure at new locations to the sensing fiber, the FBG sensor was able to better detect damage that was otherwise detected. Detailed analyses of the FBG signals and their relation to the crack growth was not performed, as the goal was to show the ability to couple new sensors using the adhesive bond.

5.5 Acknowledgement

The authors thank the Office of naval Research (ONR) (N00014-19-1-2053) for the financial support of this research.

Chapter 6

Conclusions and Recommendations for Future Work

This dissertation demonstrates and characterizes ultrasonic Lamb waves coupled from one cylindrical waveguide to another through a simple adhesive acoustic coupler. The experimental results confirm that the energy transfer from one fiber to another increases as the cross-sectional area of the waveguide increases regardless of the geometric shape, until the diameter mismatch between the two waveguides becomes too great and the energy transfer decreases due to poor contact between the waveguides. This contradicts the previous attempt to explain acoustic coupling using Coupled Mode Theory for optics, which predicted that maximum energy transfer occurs when the diameter of the input and output waveguides are identical. Also, the energy transfer increases when the modulus of elasticity matches between the two waveguides. However, the combination of the cross-sectional area and the modulus of elasticity to maximize coupling efficiency is still unknown. Later experiments confirm that the acoustic waves transferring through the adhesive coupler interfere coherently, although the degree of coherence for acoustic coupling is not estimated due to high coupling loss.

The fiber used in the coupler does not have to be a standard single-mode optical fiber, meaning the fiber exposed to the environment for extraction of signal does not have to be a standard single-mode optical fiber. This opens more opportunities for sensing applications because the fiber can be tuned or modified to react differently to the environment. Then the last experiments confirm that an already installed FBG sensing system can be easily extended to cover larger areas by attaching a segment of fiber to the environment and coupling it to the FBG fiber using the simple adhesive coupler.

FEA model simulation showed that the Spring Model has a potential to properly characterize the behavior of acoustic coupling from one optical fiber to another via adhesive coupler. The Spring Model properly modeled the energy transfer behavior, even between waveguides of different diameters. However, the Spring Model is limited to ideal case scenarios, and it cannot properly model the energy transfer decrease caused by huge diameter mismatch between the two waveguides. Also, the Spring Model is designed to describe energy transfer behavior in two waveguides that are in contact, so it cannot properly model the damping caused by the adhesive coupler that is holding the two fibers together. Therefore, future work could investigate on improving the Spring Model by adding attenuation so that it could incorporate the damping caused by the coupler material.

REFERENCES

1. Betz, D. C., Thursby, G., Culshaw, B., and Staszewski, W. J., "Acousto-ultrasonic sensing using fiber Bragg gratings," Smart Mater. Struct., 12(1), pp. 122-128. 2003 DOI: 10.1088/0964-1726/12/1/314.
2. Cuc, A. and Giurgiutiu, V., "Structural Health Monitoring with Piezoelectric Wafer Active Sensors for Space Applications," AiAA Journal, 45(12), pp. 2838-2850, 2007.
3. Alleyne, D.N. and Cawley, P., "The interaction of Lamb waves with defects," IEEE, 39(3), pp 381-397, 1992.
4. Ghadami, A., Behzad, and M., Mirdamadi, H.R., "Damage identification in multi-step waveguides using Lamb waves and scattering coefficients," Arch. Appl. Mech., 88, pp. 1009-1026, 2018.
5. Perez, I.M., Cui, H., and Udd, E., "Acoustic emission detection using fiber Bragg gratings," proc. Of SPIE, 4328, pp. 209-216, 2001.
6. Tsuda, H., "Ultrasound and damage detection in CFRP using fiber Bragg grating sensors," Composites Science and Technology, 66(5), pp. 676-683, 2006.
7. Frieden, J., Cugnoni, J., Botsis, J., and Gmur, T., "Low energy impact damage monitoring of composites using dynamic strain signals from FBG sensors – Part I: Impact detection and localization," Composite Structures, 94(2), pp. 438-445, 2012.
8. Soman, R., Wee, J., and Peters, K., "Optical Fiber Sensors for Ultrasonic Structural Health Monitoring: A Review," Sensors, 21(21), 2021.
9. Peters, K., "Fiber Bragg grating sensors," Encyclopedia of Structural Health Monitoring, 2009.

10. Wee, J., Wells, B., Hackney, D., Bradford, P., and Peters, K., “Increasing signal amplitude in fiber Bragg grating detection of Lamb waves using remote bonding,” Appl. Opt. 55, pp. 5564-5569, 2016.
11. Wee, J., Hackney, D., Bradford, P., and Peters, K., “Simulating increased Lamb wave detection sensitivity of surface bonded fiber Bragg grating,” Smart Mater. Struct. 26, 045034, 2017.
12. Matthews, A.L., Murphy, K.A., Rogers, R.E., and Claus, R.O., “Acoustic fiber waveguide coupler,” Ultrasonic Symposium, pp. 629-631, 1987.
13. Chang, J., Wang, Q., Zhang, X., Ma, L., Liu, T., Wang, Q., Liu, Z., Zhang, S., and Ding, S., “Single-end vibration sensor based on an over-coupled fiber-loop reflector,” Laser Phys. 18, 452, 2008.
14. Chang, J., Ma, L., Liu, T., Wang, H., Huo, D., Ni, J., and Shi, Z., “Fiber optic vibration sensor based on over0coupled fused coupler,” Proc. SPIE 6595, 65954C, 2007.
15. Chen, R., Fernando, G.F., Butler, T., and Badcock, R.A., “A novel ultrasound fibre optic sensor based on a fused-tapered optical fiber coupler,” Meas. Sci. Technol. 15, pp. 1490-1495, 2004.
16. Li, F., Liu, Y., Wang, L., and Chen, Y., “Anslysis of the coupling optical fiber ultrasonic sensor for partial discharge detection,” in IEEE 11th International Conference on the Properties and Applications of Dielectric Materials, 2015.
17. Wang, S., Lu, P.,Zhang, L., Liu, D., and Zhang, J., “ Optical fiber acoustic sensor based on nonstandard fused coupler and aluminum foil,” IEEE Sens. J. 14, pp. 2293-2298, 2014.
18. Birks, T.A., Russel, P.St.J., and Culverhouse, D.O., “The acousto-optic effect in single-mode fiber tapers and couplers,” J. Lightwave Technol. 14, pp. 2519-2529, 1996.

19. Leal, W.A., Carneiro, M.B.R., Freitas, T.A.M.G., Marcondes, C.B., and Ribeiro, R.M., "Low-frequency detection of acoustic signals using fiber as an ultrasonic guide with a distant in-fiber Bragg grating," Microw. Opt. Technol. Lett. 60, pp. 813-817, 2018.
20. Saffai-Jazi, A., "Analysis and design of acoustic fiber coupler," in Ultrasonic Symposium, pp. 433-437, 1987.
21. Wu, Q., Okabe, Y., and Yu, F., "Ultrasonic structural health monitoring using fiber Bragg grating," Sensors 18, 3395, 2018.
22. Wee, J. and Peters, K., "Laser Doppler vibrometry measurements of conversion of surface guided waves to optical fiber modes," IEEE Photon. Technol. Lett. 32, pp. 349-352, 2020.
23. Marashi, C., "Acoustic wave coupling through adhesively bonded optical fibers," North Carolina State University, unpublished data.
24. Thurston, R.N., "Elastic waves in rods and clad rods," J. Acoust. Soc. Am. 64, pp. 1-37, 1978.
25. Lee, J.R. and Tsuda, H., "Sensor application of fibre ultrasonic waveguide," Meas. Sci. Technol. 17, pp 645-652, 2006.
26. Seco, F. and Jimenez, A.R., "Modeling the generation and propagation of ultrasonic signals in cylindrical waveguides," in Ultrasonic Waves, DrSantos, ed. Pp. 1-28, InTech, 2012.
27. Tsuda, H., Sato, E., Nakajima, T., Nakamura, H., Arakawa, T., Shiono, H., Minato, M., Kurabayashi, H., and Sato, A., "Acoustic emission measurement using a strain-insensitive fiber Bragg grating sensor under varying load conditions," Opt. Lett. 34, pp. 2942– 2944, 2009.
28. Lee, J.R. and Tsuda, H., "Fiber optic liquid leak detection technique with an ultrasonic actuator and a fiber Bragg grating," Opt. Lett. 30, pp. 3293–3295, 2005.

29. Muc, S., Gudra, T., and Bereś-Pawlik, E., “Experimental Study of Simultaneous Transmission of Ultrasonic Waves and Optical Radiation via Optical Fiber Couplers,” Arch. Acoust. 35, pp. 111–122, 2010.
30. Kim, J.M., Marashi, C., Wee, J., Peters, K., “Acoustic wave coupling between optical fibers of different geometries,” Appl. Opt. 60, 11042, 2021.
31. Dai, Y., Li, P., Liu, Y., Asundi, A., and Leng, J., “Integrated real-time monitoring system for strain/temperature distribution based on simultaneous wavelength and time division multiplexing technique,” Opt. Lasers Eng. 59, pp. 19–24, 2014.
32. Luo, Z., Wen, H., Guo, H., and Yang, M., “A time- and wavelength-division multiplexing sensor network with weak fiber Bragg gratings,” Opt. Express 21, 22799–22807, 2013.
33. Liu, W., Guan, Z.-G., Liu, G., Yan, C., and He, S., “Optical low-coherence reflectometry for a distributed sensor array of fiber Bragg gratings,” Sens. Actuators A 144, pp. 64–68, 2008.
34. Guan, Z.G., Chen, D., and He, S., “Coherence Multiplexing of Distributed Sensors Based on Pairs of Fiber Bragg Gratings of Low Reflectivity,” J. Lightwave Technol. 25, pp. 2143–2148, 2007.
35. Hotate, K. and He, Z., “Synthesis of Optical-Coherence Function and Its Applications in Distributed and Multiplexed Optical Sensing,” J. Lightwave Technol. 24, pp. 2541–2557, 2006.
36. Youngquist, R.C., Malocha, D., and Saldanha, N., “Surface Acoustic Wave Tag-Based Coherence Multiplexing,” U.S. Patent No. 9,477,857, 25 October 2016; U.S. Patent and Trademark Office: Alexandria, VA, USA, 2016. Available online: https://ntrs.nasa.gov/citations/20160013206 (accessed on 29 May 2022). Ryzy, M.;

Grabec, T.; Österreicher, J.A.; Hettich, M.; Veres, I.A. Measurement of coherent surface acoustic wave attenuation in polycrystalline aluminum. AIP Adv. 2019, 8, 125019.

37. Ryzy, M., Grabec, T., Österreicher, J.A., Hettich, M., and Veres, I.A., "Measurement of coherent surface acoustic wave attenuation in polycrystalline aluminum," AIP Adv. 8, 125019, 2019.
38. Xu, R., Liu, S., Sun, Q., Lu, P., and Liu, D., "Experimental characterization of a Vernier strain sensor using cascaded fiber rings," IEEE Photon. Technol. Lett. 24, pp. 2125–2128, 2012.
39. Magalhaes, R., Silva, S.O., and Frazão, O., "Fiber ring resonator using a cavity ring-down interrogation technique for curvature sensing." Microw. Opt. Technol. Lett. 58, pp. 267–270, 2016.
40. Zhang, L., Lu, P., Chen, L., Huang, C., Liu, D., and Jiang, S., "Optical fiber strain sensor using fiber resonator based on frequency comb Vernier spectroscopy," Opt. Lett. 37, pp. 2622–2624, 2012.
41. Presti, D., Videla, F.A., and Torchia, G.A., "Optical fiber ring resonator as a high-resolution spectrometer. Characterization and applications with single line diode lasers," Opt. Eng. 57, 057108, 2018.
42. Ying, D., Ma, H., and Jin, Z., "Ringing phenomenon of the fiber ring resonator," Appl. Opt. 46, pp. 4890–4895, 2007.
43. Wu, Q., Yu, F., Okabe, T., and Kobayashi, S., "Application of a novel optical fiber sensor to detefction of acoustic emissions by various damages in CFRP laminates," Smart Materials and Structures, 24(1), 2015.

44. Kim, J.M., Wee, J., and Peters, K., “Demonstration of Coherent Interference between Acoustic Waves Using a Fiber Ring Resonator,” Sensors 22(4163), 2022.

45. Haag, T., Beadle, B.M, Sprenger, H., and Gaul, L., “Wave-based defect detection and interwire friction modeling for overhead transmission lines,” Arch. Appl. Mech 79, pp. 517-528, 2009.

46. Schaal, C., Bischoff, S., and Gaul, L., “Energy-based models for guided ultrasonic wave propagation in multi-wire cables,” International Journal of Solids and Structures, 64-65, pp. 22-29, 2015.

47. Zhang, P., Tang, Z., Lv, F., and Yang, K., “Numerical and Experimental Investigation of Guided Wave Propagation in a Multi-Wire Cable,” Appl. Sci., 9, 1028, 2019.

48. Hayle, S.T., Manie, Y.C., Dehnaw, A.M., Hsu, Y.T., Li, J.W., Liang, H.C., and Peng, P.C., “Reliable self-healing FBG sensor network for improvement of multipoint strain sensing,” Optics Communications 499, pp. 127286, 2021.